

MEASUREMENTS OF DYNAMIC PROPERTIES OF MATERIALS

Volume V
OFHC COPPER
FINAL REPORT

AD 728846

by

D. R. Christman
W. M. Isbell
S. G. Babcock

Materials and Structures Laboratory
Manufacturing Development, General Motors Corporation
General Motors Technical Center, Warren, Michigan 48090

Reproduced by
NATIONAL TECHNICAL
INFORMATION SERVICE
Springfield, Va. 22151

UNCLASSIFIED

Security Classification

DOCUMENT CONTROL DATA - R & D

(Security classification of title, body of abstract and indexing annotation must be entered when the overall report is classified)

1. ORIGINATING ACTIVITY (Corporate author) Manufacturing Development, General Motors Corporation, General Motors Technical Center, Warren, Michigan	2a. REPORT SECURITY CLASSIFICATION UNCLASSIFIED
	2b. GROUP

3. REPORT TITLE

Measurements of Dynamic Properties of Materials Volume V: OFHC Copper

4. DESCRIPTIVE NOTES (Type of report and inclusive dates)

Final Report (in Six Volumes)

5. AUTHOR(S) (First name, middle initial, last name)

Douglas R. Christman, William M. Isbell, Stephen G. Babcock

6. REPORT DATE

1971 July

7a. TOTAL NO. OF PAGES

104

7b. NO. OF REFS

58

8a. CONTRACT OR GRANT NO.

DASA-01-68-C-0114

9a. ORIGINATOR'S REPORT NUMBER(S)

MSL-70-23, Vol. V

b. PROJECT NO.

NWER XAXA

9b. OTHER REPORT NO(S) (Any other numbers that may be assigned this report)

c. Task and Subtask A106

DASA-2501-5

d. Work Unit 07

10. DISTRIBUTION STATEMENT

Approved for public release; distribution unlimited.

11. SUPPLEMENTARY NOTES

12. SPONSORING MILITARY ACTIVITY

Director

Defense Atomic Support Agency
Washington, D. C. 20305

13. ABSTRACT

Results of an experimental study on the dynamic properties of OFHC copper (1/2-hard) are presented. Areas studied included stress-strain-strain rate and reverse loading behavior, elastic constants, equation of state, compressive and release wave characteristics, and spall fracture. The material showed approximately elastic-perfectly plastic behavior under uniaxial stress compression with slight rate sensitivity (0.005 to 950/sec strain rates and 20,204 and 370°C). Longitudinal and shear wave velocities at 20°C were 4.757 and 2.247 mm/usec, and temperature and pressure dependence was also measured and various elastic constants were calculated. The shock wave equation of state (EOS) was measured from 10 to 200 kbars as $\sigma_H = 1.5 + 344 u_p + 143 u_p^2$. The EOS was also calculated from the elastic constants and comparisons made with the shock wave EOS. Compressive wave tests showed a ramped, non-steady-state elastic precursor with very rapid decay (> 80% in 2 mm). The yield level from compressive wave profile measurements was considerably lower than that determined from uniaxial stress and EOS tests. Shock wave profiles showing both release wave behavior and attenuation were obtained. The impact velocity required for spall fracture was found to increase with decreasing pulse width.

DD FORM 1473
1 NOV 65

UNCLASSIFIED

Security Classification

b6

UNCLASSIFIED

Security Classification

14. KEY WORDS	LINK A		LINK B		LINK C	
	ROLE	WT	ROLE	WT	ROLE	WT
Stress-strain-strain rate Reverse loading behavior Elastic constants Equation of State Compressive and release wave characteristics Spall fracture						

UNCLASSIFIED

Security Classification

DASA 2501-5
MSL-70-23 Vol.V
1971 July

MEASUREMENTS OF DYNAMIC PROPERTIES OF MATERIALS
Volume V
OFHC COPPER
FINAL REPORT

This work was sponsored by the Defense Atomic Support Agency under NWER Subtask AA 106"

by
D. R. Christman
W. M. Isbell
S. G. Babcock

Materials and Structures Laboratory
Manufacturing Development, General Motors Corporation
General Motors Technical Center, Warren, Michigan 48090

Prepared For
HEADQUARTERS
Defense Atomic Support Agency
Washington, D.C. 20305

Under Contract DASA01-68-C-0114

"Approved for public release; distribution unlimited"

11
COPY No. _____

ABSTRACT

Results of an experimental study on the dynamic properties of OFHC copper (1/2-hard) are presented. Areas studied included stress-strain-strain rate and reverse loading behavior, elastic constants, equation of state, compressive and release wave characteristics, and spall fracture. The material showed approximately elastic-perfectly plastic behavior under uniaxial stress compression with slight rate sensitivity (0.005 to 950/sec strain rates and 20,204 and 370°C). Longitudinal and shear wave velocities at 20°C were 4.757 and 2.247 mm/μsec, and temperature and pressure dependence was also measured and various elastic constants were calculated. The shock wave equation of state (EOS) was measured from 10 to 200 kbars as $\sigma_H = 1.5 + 344 u_p + 143 u_p^2$. The EOS was also calculated from the elastic constants and comparisons made with the shock wave EOS. Compressive wave tests showed a ramped, non-steady-state elastic precursor with very rapid decay (> 80% in 2 mm). The yield level from compressive wave profile measurements was considerably lower than that determined from uniaxial stress and EOS tests. Shock wave profiles showing both release wave behavior and attenuation were obtained. The impact velocity required for spall fracture was found to increase with decreasing pulse width.

MSL-70-23, Vol. V

FOREWORD - EXPERIMENTAL DATA VOLUMES

The prediction of reentry vehicle response to impulsive loading resulting from energy deposition has been studied extensively during the last decade. Analytical models and computer routines have been developed to assess the vulnerability of such vehicles to the initial loading phase, in which stress waves are generated and propagated through the structure, and to subsequent phases, where elastic vibration, plastic deformation and/or fracture may occur.

A Defense Atomic Support Agency (DASA) program was initiated with the objective of improving computer codes for the prediction of damage induced by X-rays (PREDIX). The PREDIX metals program has combined the efforts of several contractors under the direction of DASA. The primary contributions of each contractor can be summarized as follows:

General Motors Corporation--Measurement of material properties, including stress-strain-strain rate behavior, elastic constants, equations of state, shock wave profiles and spall fracture.

Effects Technology Inc.--Spall fracture tests and analysis (exploding foil) and underground testing.

KMS Technology Center--Constitutive modeling.

Physics International Company--Energy deposition and spall fracture studies (electron beam).

Systems, Science and Software--Energy deposition and front surface phenomena, constitutive modeling and code development, and underground testing.

TABLE OF CONTENTS

	<u>Page</u>
ABSTRACT	iii
FOREWORD	iv
LIST OF ILLUSTRATIONS	vii
LIST OF SYMBOLS	ix
INTRODUCTION	1
SECTION I - MATERIAL PROPERTIES	3
SECTION II - STRESS-STRAIN STUDIES	7
Uniaxial Stress Tests	7
Reverse Loading Tests	13
SECTION III - ELASTIC BEHAVIOR	17
Wave Velocity Measurements	17
Elastic Constants	19
Gruneisen Parameter	20
Debye Temperature	23
SECTION IV - EQUATION OF STATE	25
Shock Wave Equation of State	25
Ultrasonic Equation of State	34
Yield Behavior	38
Metallographic Studies	41
SECTION V - WAVE PROPAGATION	44
Compressive Wave Behavior	44
Release Waves and Wave Attenuation	52
SECTION VI - SPALL FRACTURE	58
Recovery Tests	58
Spall Profiles	67

TABLE OF CONTENTS (Continued)

	<u>Page</u>
SUMMARY	70
ACKNOWLEDGMENT	73
REFERENCES	74
APPENDIX A - ELASTIC CONSTANTS EQUATIONS	79
APPENDIX B - GRUNEISEN PARAMETER ESTIMATES	83
APPENDIX C - GRUNEISEN PARAMETER, PRESSURE DERIVATIVE	87
APPENDIX D - DEVIATORIC STRESS ESTIMATES	90
APPENDIX E - EQUATIONS OF STATE, ULTRASONICS	93
DISTRIBUTION LIST	96
DD FORM 1473 DOCUMENTATION CONTROL - R&D	103

LIST OF ILLUSTRATIONS

<u>Figure</u>	<u>Page</u>
1 OFHC Copper, 63.5 mm Diameter Bar Stock	4
2 As-Received and Annealed OFHC Copper	6
3 Compressive Stress vs Strain, Copper	8
4 Compressive Stress vs Log Strain Rate, Copper (20°C)	11
5 Compressive Yield Stress vs Log Strain Rate, Copper (20°C)	12
6 Reverse Loading Tests in Copper, Strain Effects	14
7 Reverse Loading Tests in Copper, Cyclic Effects	16
8 Quartz Gage Records	26
9 Streak Camera Record, "Hat" Target	28
10 Stress-Particle Velocity Hugoniot, Copper	30
11 Stress or Mean Pressure - Compression Hugoniot, Copper	31
12 Shock Velocity-Particle Velocity Hugoniot, Copper	32
13 Shock Wave Test Specimens, Copper	42
14 As-Received and Shock-Loaded Copper Foils, Transmission Electron Micrographs	43
15 Compressive Waves, Propagation Distance Dependence	45
16 Compressive Waves, Peak Stress Dependence	47
17 Compressive Waves, 1/2 Hard and Annealed Material	48

LIST OF ILLUSTRATIONS (Continued)

<u>Figure</u>		<u>Page</u>
18	Elastic Precursor Decay in Copper	51
19	Effect of Tilt on Quartz Gage Records	53
20	Wave Profiles, Stress Dependence	55
21	Wave Attenuation in Copper	57
22	Spall Fractures in Copper (1.5 mm → 3.0 mm)	60
23	Spall Fractures in Copper	61
24	Spall Fractures in Metals	62
25	Spall Fractures in Copper (1.5 mm → 3.0 mm, 0.115 mm/μs)	64
26	Spall Fracture Surface in Copper (0.5 mm → 1.0 mm, 0.181 mm/μs)	64
27	Spall Data for Copper	65
28	Spall Wave Profiles in Copper (1 mm → 2.5 mm)	68
29	Attenuated Spall Wave Profile in Copper	69

LIST OF TABLES

<u>Table</u>		<u>Page</u>
I	Elastic Constants for Copper (P=0, T=20°C)	21
II	Equations of State Comparison-Hydrostat	37
III	Velocity Interferometer Test Data (20°C)	54
IV	Incipient Spall Data for Copper (20°C)	66

LIST OF SYMBOLS

c_B	Bulk Wave Velocity, mm/ μ sec
c_L	Longitudinal Wave Velocity, mm/ μ sec
c_S	Shear Wave Velocity, mm/ μ sec
c_p	Specific Heat, cal/g
G	Shear Modulus, kbar
K	Bulk Modulus, kbar
P_H	Mean Pressure, Hydrostat, kbar
P_S	Mean Pressure, Adiabat, kbar
P_T	Mean Pressure, Isotherm, kbar
T	Temperature, °C
U_S	Shock Wave Velocity, mm/ μ sec
u_p	Particle Velocity, mm/ μ sec
v	Specific Volume, cc/g
V_I	Impact Velocity, mm/ μ sec
x	Target Thickness, mm
x_O	Impactor Thickness, mm
x^S	Adiabatic Modulus, kbar
x^T	Isothermal Modulus, kbar
x_{OS}^S, x_{OS}^T	Adiabatic Pressure Derivative @ Zero Pressure $\left(= \left(\frac{\partial x^S}{\partial P} \right) S \Big _{P=0} \right)$
x_{OT}^T, x_{OT}^S	Isothermal Pressure Derivative @ Zero Pressure $\left(= \left(\frac{\partial x^T}{\partial P} \right) T \Big _{P=0} \right)$
β	Volume Coefficient of Expansion, /°C $= - \frac{1}{\rho} \left(\frac{\partial \rho}{\partial T} \right)_{P=0}$

MANUFACTURING DEVELOPMENT • GENERAL MOTORS CORPORATION

MSL-70-23, Vol. V

LIST OF SYMBOLS (Continued)

γ	Gruneisen Parameter
μ	Compression ($= v_0/v - 1$)
ν	Poisson's Ratio
ρ	Density, g/cc
σ_H	Stress, Hugoniot, kbar

INTRODUCTION

This report is one of a series of six giving results of a study of dynamic properties of materials. The principle objectives of this study were:

- Provide measurements of dynamic properties of materials to be used as inputs to model development for shock wave propagation and dynamic fracture.
- Provide data to establish accuracy of computer code predictions.
- Provide physical interpretation of experimentally observed material response to dynamic test conditions.

The primary areas studied included: (1) Stress-strain-strain rate behavior in uniaxial stress, including Bauschinger effect; (2) Elastic constants, including temperature and pressure dependence; (3) Hugoniot equation of state; (4) Compressive and release wave profiles, including elastic precursor decay and wave attenuation; and (5) Spall fracture studies, including pulse width dependence. The six reports in this series are:

Vol. I: Summary of Results, DASA 2501-1 (AD712847)
Vol. II: Experimental Methods and Techniques,
 DASA 2501-2
Vol. III: 6061-T6 Aluminum, DASA 2501-3
Vol. IV: Alpha Titanium, DASA 2501-4
Vol. V: OFHC Copper, DASA 2501-5
Vol. VI: Tantalum, DASA 2501-6

MSL-70-23, Vol. V

The experimental techniques utilized in this study are reviewed in Vol. II (DASA 2501-2). Briefly, the principal techniques applied were:

Stress-strain Studies--A laboratory-type universal testing machine was used for rates $< 0.1/\text{sec}$, a medium strain rate machine for rates of $10^{-3}/\text{sec}$ to $10^2/\text{sec}$, and a Hopkinson bar device for rates of about 10^2 to $5 \times 10^3/\text{sec}$.

Elastic Constants--The pulse superposition method was used for measuring longitudinal and shear wave velocities as functions of temperature and hydrostatic pressure.

Equation of State--Gun-launched, flat-plate impact techniques were used to generate uniaxial strain conditions. Velocities up to $0.6 \text{ mm}/\mu\text{sec}$ were achieved with 63.5 mm and 102 mm single-stage compressed-gas guns, and velocities of 0.3 to 2 $\text{mm}/\mu\text{sec}$ were achieved with a 64 mm single-stage, powder gun. Hugoniot data were obtained with x-cut quartz gage and streak camera techniques.

Wave Propagation and Spall Fracture--Flat-plate impact techniques were also used. Wave profiles were measured with x-cut quartz gages and a laser velocity interferometer.

A literature search on dynamic properties of materials was carried out under the PREDIX program and a listing of recent publications (including abstracts) on dynamic properties of materials is given in Reference 1.

SECTION I

MATERIAL PROPERTIES

Copper has a face-centered-cubic structure and the material on which tests discussed in this report were carried out is an oxygen-free, high-conductivity (OFHC^{*}) grade certified to be 99.99% minimum copper. Chemical analysis identified no other elements present in amounts greater than 0.0005%. This copper is not heat-treatable and different strength levels are achieved by cold-working. The material tested was purchased as 63.5 mm diameter bar stock, which was found to be preferable to plate stock since it puts essentially no limit on specimen thickness and gives little scrap while ensuring that all specimens are from the same parent material.

The copper bar stock was nominally 1/2-hard, which corresponds to a handbook tensile yield strength of \sim 2.5 kbar at a "static" test rate. Measured hardness was 78R_F (equivalent to \sim 74 Brinell @ 500 kg load). A photomicrograph of a representative portion of the bar is shown in Figure 1. The bar axis or centerline is vertical in this picture and the width shown is \sim 4 mm out of a total of 63.5 mm. There is some grain elongation along the axis with about a factor of three variation in grain size, the average being approximately ASTM 5 (64 μ m). For results presented in this report, the test or wave propagation direction was axial (i.e., vertical in Figure 1).

The measured density (ρ_0) of the copper was 8.917 g/cc (0.322 lb/in.³). For use in equation of state and energy

* Trade Mark, American Metal Climax, Inc.

MSL-70-23, Vol. V

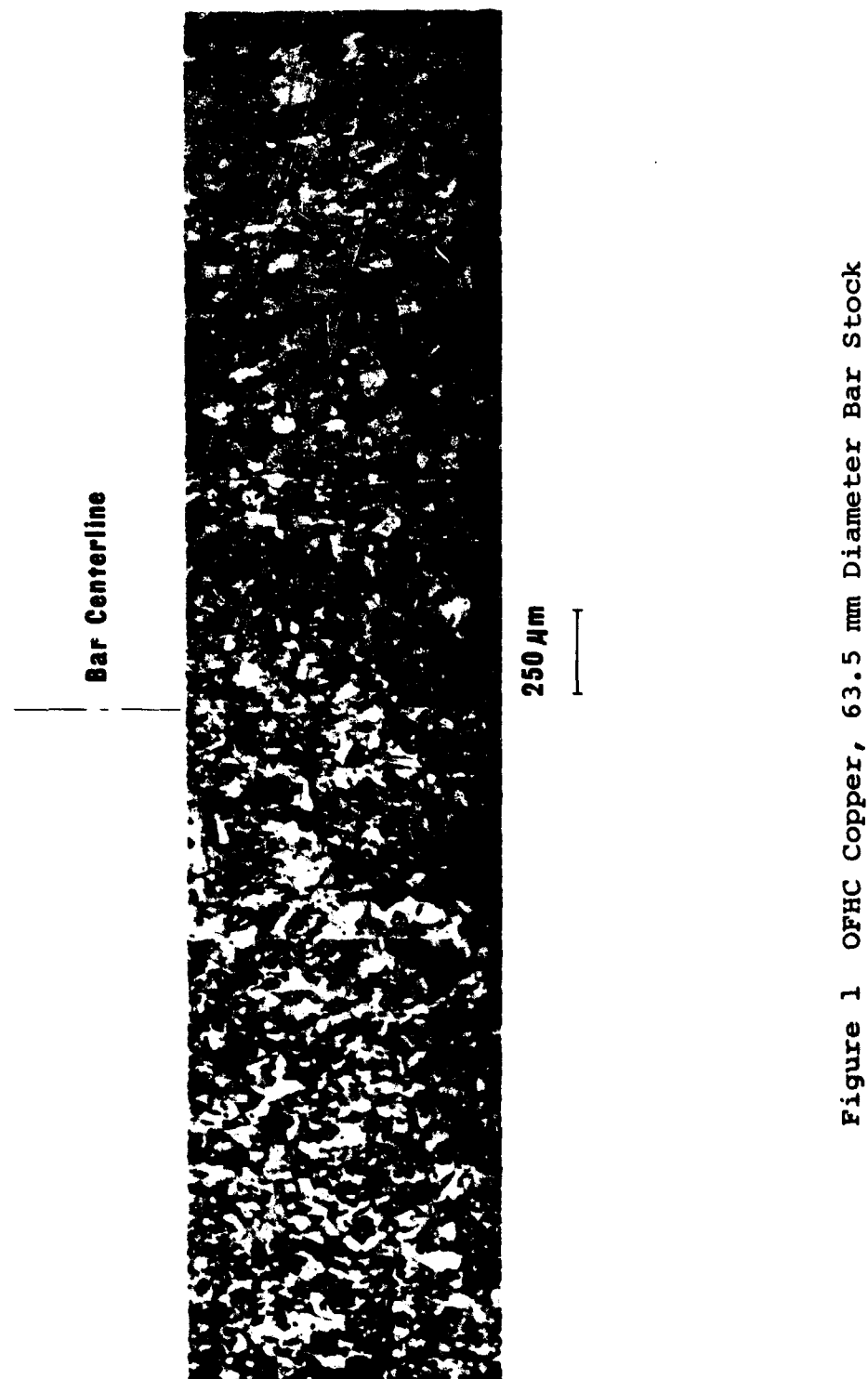


Figure 1 OFHC Copper, 63.5 mm Diameter Bar Stock

deposition calculations, several physical constants were compiled from the literature⁽²⁻⁴⁾ and are listed below:*

Volume coefficient of thermal expansion, β :

$$51.5 \times 10^{-6} + 0.006 \times 10^{-6} \times T / ^\circ C$$

Specific heat, c_p :

$$0.0915 + 0.00003 \times T \text{ cal/g}$$

Melting temperature: 1080°C

Boiling temperature: 2595°C

Latent heat of fusion: 49 cal/g

Latent heat of vaporization: 1146 cal/g

(T in °C)

A portion of the copper bar was annealed for use in some stress-strain and compressive wave tests. Grain structure of the annealed material is compared with as-received stock in Figure 2. The annealing treatment was 1 hour at 500°C in air, followed by air cooling. Hardness after annealing and machining away of the oxidized surface layer was 35 R_F.

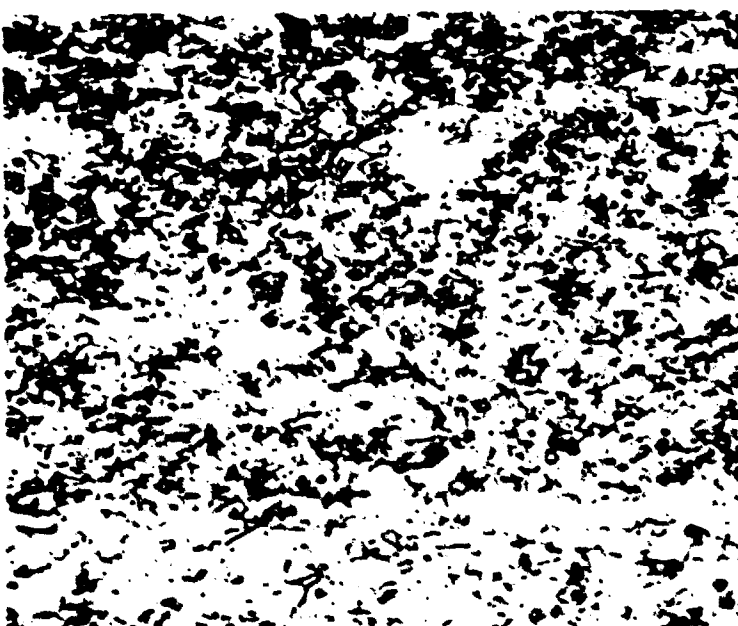
* A very thorough compilation of thermodynamic and elastic constants for the elements is given by K. A. Gschneidner in Solid State Physics, Vol. 16, 1964. The constants listed above generally differ slightly from those given by Gschneidner due to consideration of more recent data.

MSL-70-23, Vol. V

$R_F = 35$



$R_F = 78$



AS-RECEIVED
(1/2 HARD)

ANNEALED
(1 HR. @ 500°C)

Figure 2 As-Received and Annealed OFHC Copper

SECTION II

STRESS-STRAIN STUDIES

Shock wave and structural response code input requirements include constitutive equations relating stress to strain and to strain rate. To obtain these, measurements are made of uniaxial compressive stress vs. strain at various strain rates and temperatures. These tests give yield and flow stress behavior, strain rate sensitivity and work hardening characteristics. Although it is recognized that heating rate and time-at-temperature, as well as final temperature, are important in assessing material properties under short-time ($< 10^{-6}$ sec) energy-deposition conditions, the stress-strain data reported here are for relatively long heating times only. Bauschinger effect tests were conducted to provide information on unloading and subsequent yield.

UNIAXIAL STRESS TESTS

Results of compressive stress-strain tests on copper are shown in Figure 3 for strain rates of 0.005/sec to 950/sec, with each curve the average of several tests. The as-received copper was tested at three temperatures (20, 204 and 370°C), while a few tests were performed on annealed material at 20°C. The heating rate for the elevated temperature tests was ~ 0.5 °C/sec, and the reduction in yield and flow stress observed at elevated temperature may be a function of heating rate, as has been observed for 6061-T6 aluminum. (5)

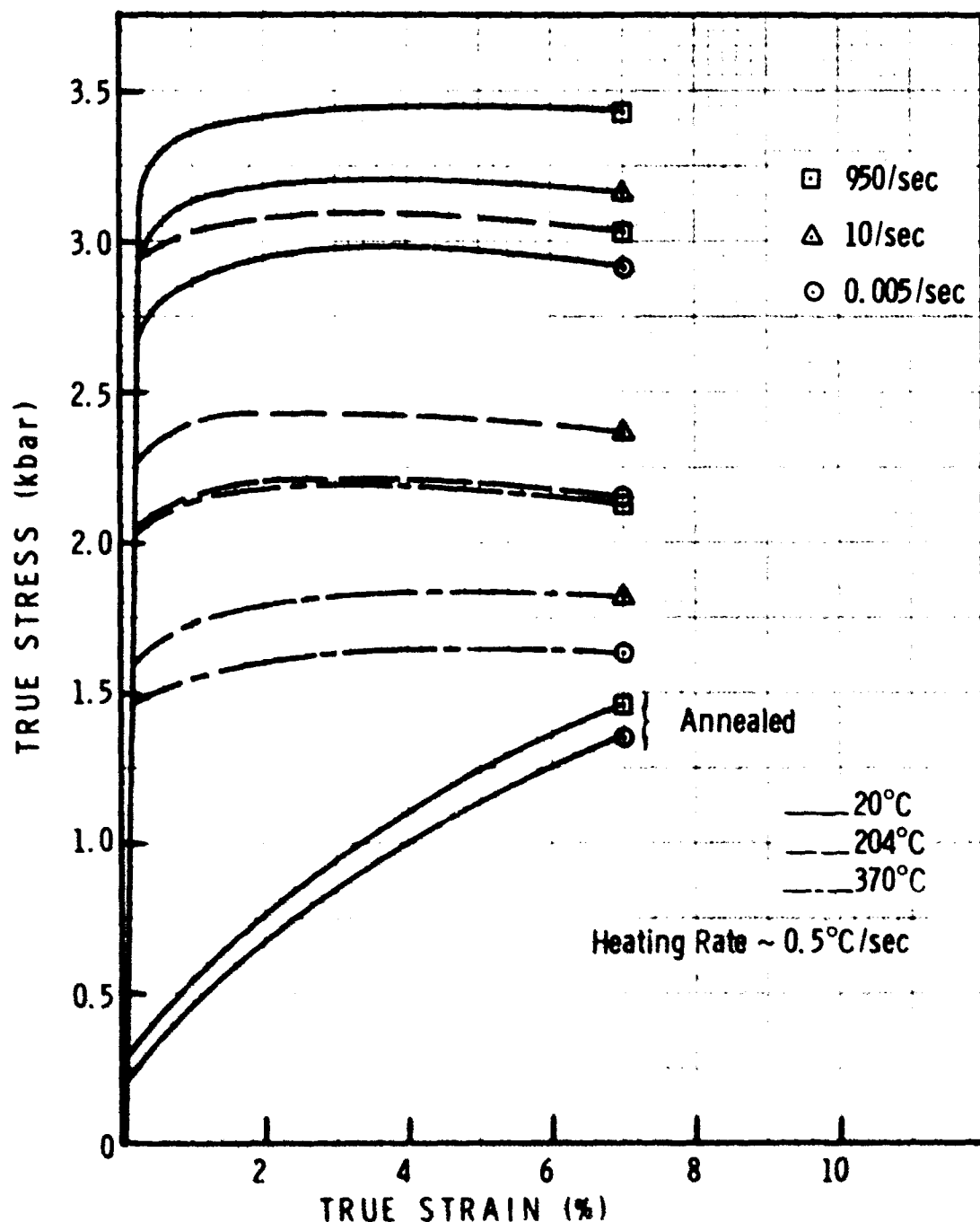


Figure 3 Compressive Stress vs Strain, Copper

The strain rates given are average plastic strain rates, with strain rate variation during the test less than a factor of two in the plastic region. The effect of this variation has been shown⁽⁶⁾ to be insignificant when considering six or seven orders of magnitude range in strain rate. Accuracy of the results is $\pm 3\%$ for low and intermediate rates and $\pm 10\%$ for the high rate. Repeatability was better, however, and scatter due to material variability and technique error was less than 2% for low and intermediate rates, and less than 4% for the high rate above 2% strain.

The stress-strain curves in Figure 3 for as-received (1/2-hard) copper show an elastic-plastic behavior with very little work hardening, at all strain rates and temperatures studied. The annealed copper shows an order of magnitude decrease in yield strength but a pronounced increase in work hardening. Work hardening exponents, N , were calculated from the compressive stress-strain curves by applying the following relation to the plastic region:

$$\sigma = \sigma_y \left(\frac{\epsilon}{\epsilon_y} \right)^N \quad (1)$$

where σ and ϵ are stress and strain at a given point in the plastic region and σ_y and ϵ_y are stress and strain at yield.

By taking σ and ϵ at 4% true strain and assuming the stress-strain curve between yield and 4% strain is linear on a log-log basis, the following strain hardening exponents were obtained:

MSL-70-23, Vol. V

<u>Material</u>	<u>Strain Rate (Per Sec)</u>	<u>N (@ 4% Strain)</u>
Cu, 1/2-hard	0.005	0.038
Cu, 1/2-hard	950	0.031
Cu, Annealed	0.005	0.29
Cu, Annealed	950	0.27

Strain rate behavior is summarized in the cross plots given in Figures 4 and 5. The as-received material shows a slight rate sensitivity up to 10^3 /sec at 20°C, while the yield and flow stresses for the annealed material are influenced very little (on an absolute scale) by strain rate. At elevated temperatures, there is a noticeable increase in the sensitivity at rates above 10/sec.

Analysis of strain rate effects under uniaxial stress conditions in copper by Kumar and Kumble⁽⁷⁾ has indicated that at low rates (< 10/sec) flow stress is controlled by thermal activation of mobile dislocations, primarily over forest dislocation barriers. At higher rates (> 10^3 /sec), dislocation motion becomes viscous phonon drag limited. They also concluded that mobile dislocation density at high rates is strain rate independent.

Although deformation twinning in shock-loaded copper (see Equation of State discussion below) has been observed, no experimental evidence of twinning in the uniaxial stress tests was found.⁽⁸⁾ Also, plain-strain compression tests on annealed, single-crystal copper by Wonsiewicz and Chin⁽⁹⁾ revealed no evidence of twinning. Their tests showed large strength differences (factor of three) in true stress-true strain curves for various crystal orientations. However, when presented as shear stress-shear strain curves and corrected for crystal rotation, the curves overlapped in a relatively narrow band.

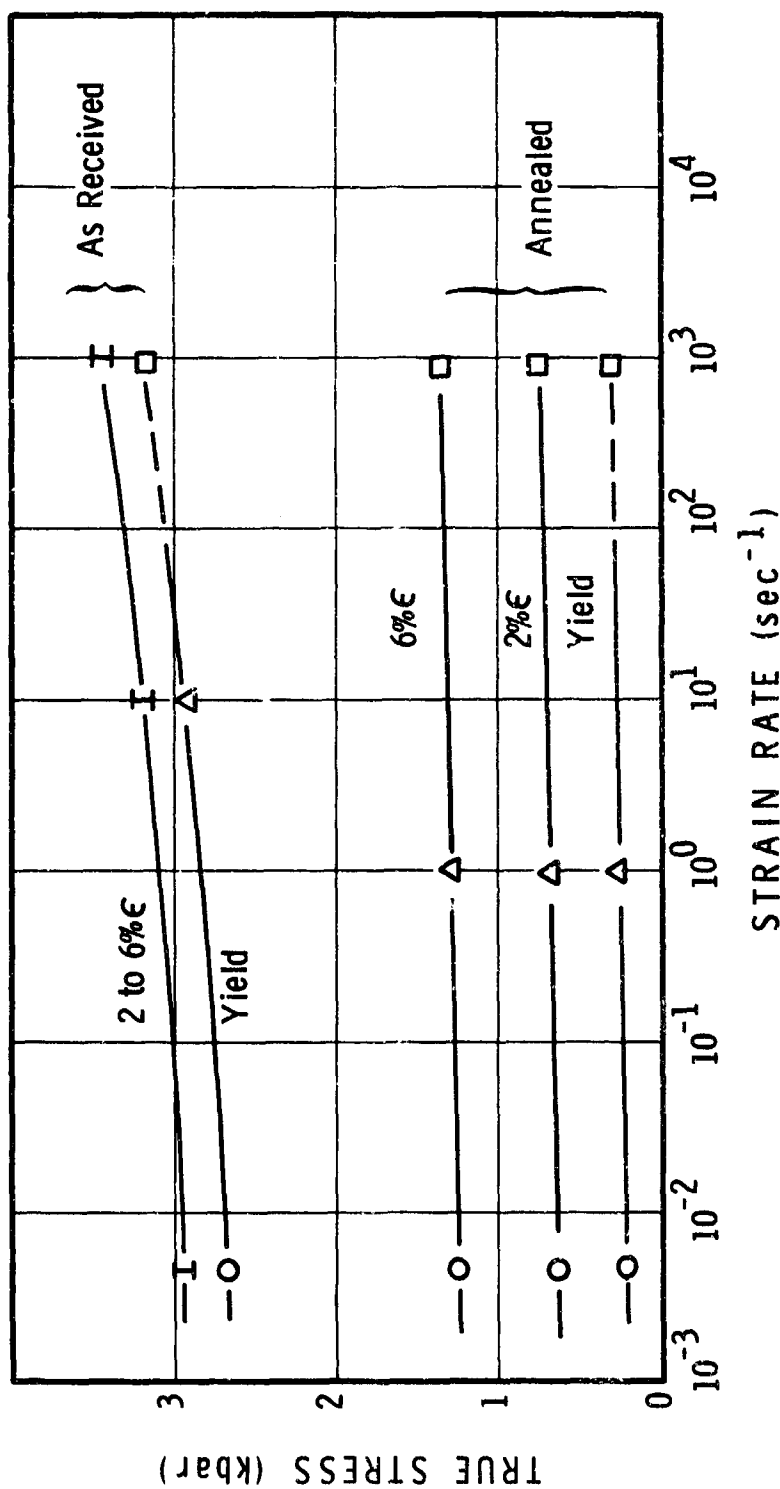


Figure 4 Compressive Stress vs Log Strain Rate, Copper (20°C)

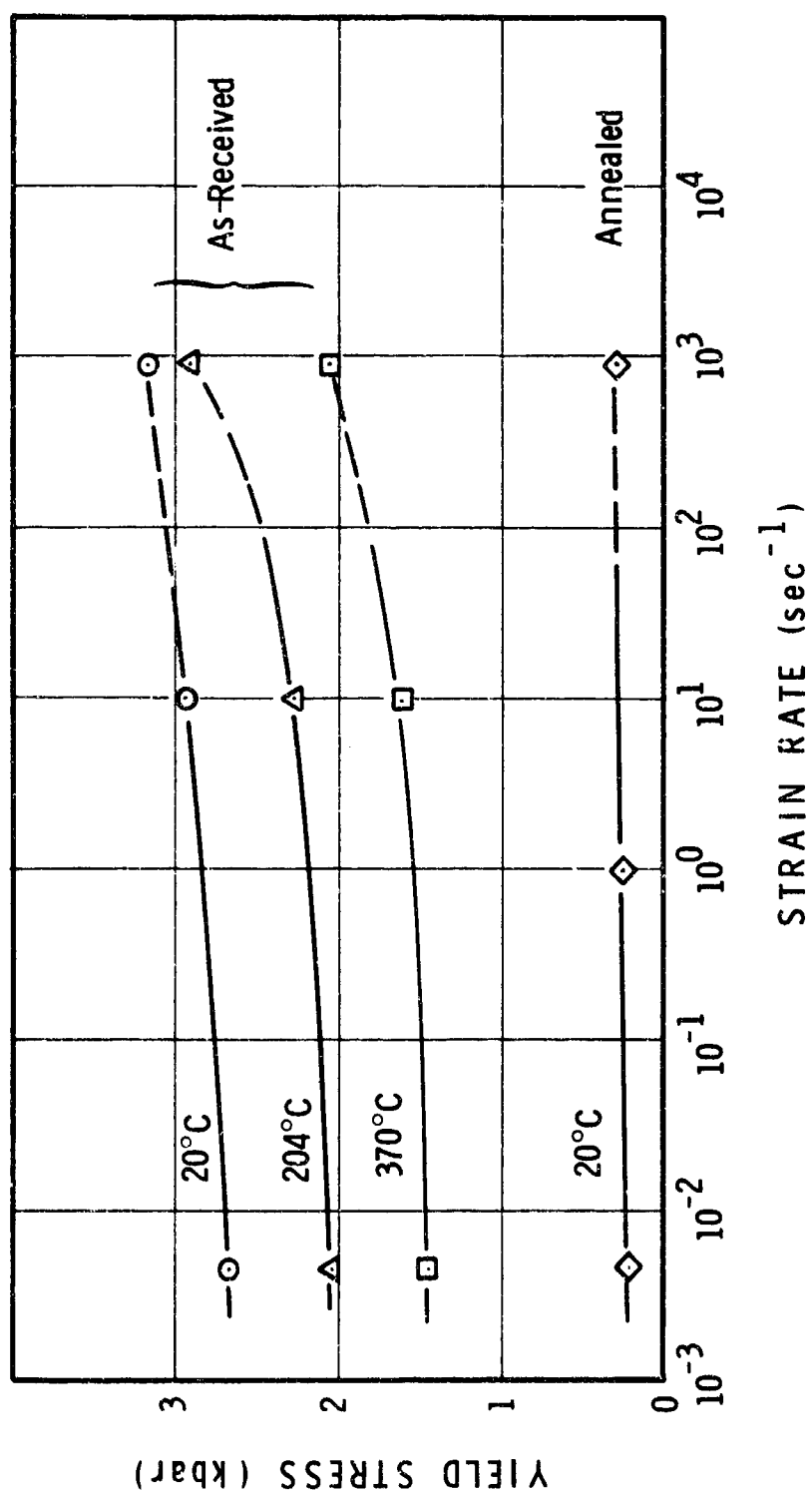


Figure 5 Compressive Yield Stress vs Log Strain Rate, Copper (20°C)

All data presented in Figures 3 to 5 are for a test direction parallel to the bar axis. A few tests conducted normal to the axis showed the flow stress to be ~ 0.25 kbar higher, with rate sensitivity and strain hardening behavior about the same.

REVERSE LOADING TESTS

The reverse loading behavior or Bauschinger effect* was studied by performing uniaxial tensile stress tests after the material had been prestrained in the opposite (compressive) sense. Two variations of this method of determining the Bauschinger effect were used:

1. Uniaxial stress specimens were loaded in compression to strains of 0.5 to 3.0%, unloaded to zero stress, and then immediately loaded in tension.
2. Specimens were compression-tension cycled several times with a total plastic strain of 1% per cycle.

The materials were deformed at room temperature and at a strain rate of 10^{-3} /sec in the above experiments. The results of the first tests are shown in Figure 6. The Bauschinger strain (defined here as the plastic strain in the reverse loading path at 3/4 of the initial yield strength) increases slightly with increasing prestrain. No evidence of any plastic deformation during unloading was seen. However, plastic deformation during unloading has been observed at strains less than 0.5% with measurement sensitivities much greater than those in the present experiments.

* The Bauschinger effect is the reduction in stress at a given strain in the reverse direction compared to that in the original loading direction.

MSL-70-23, Vol. V

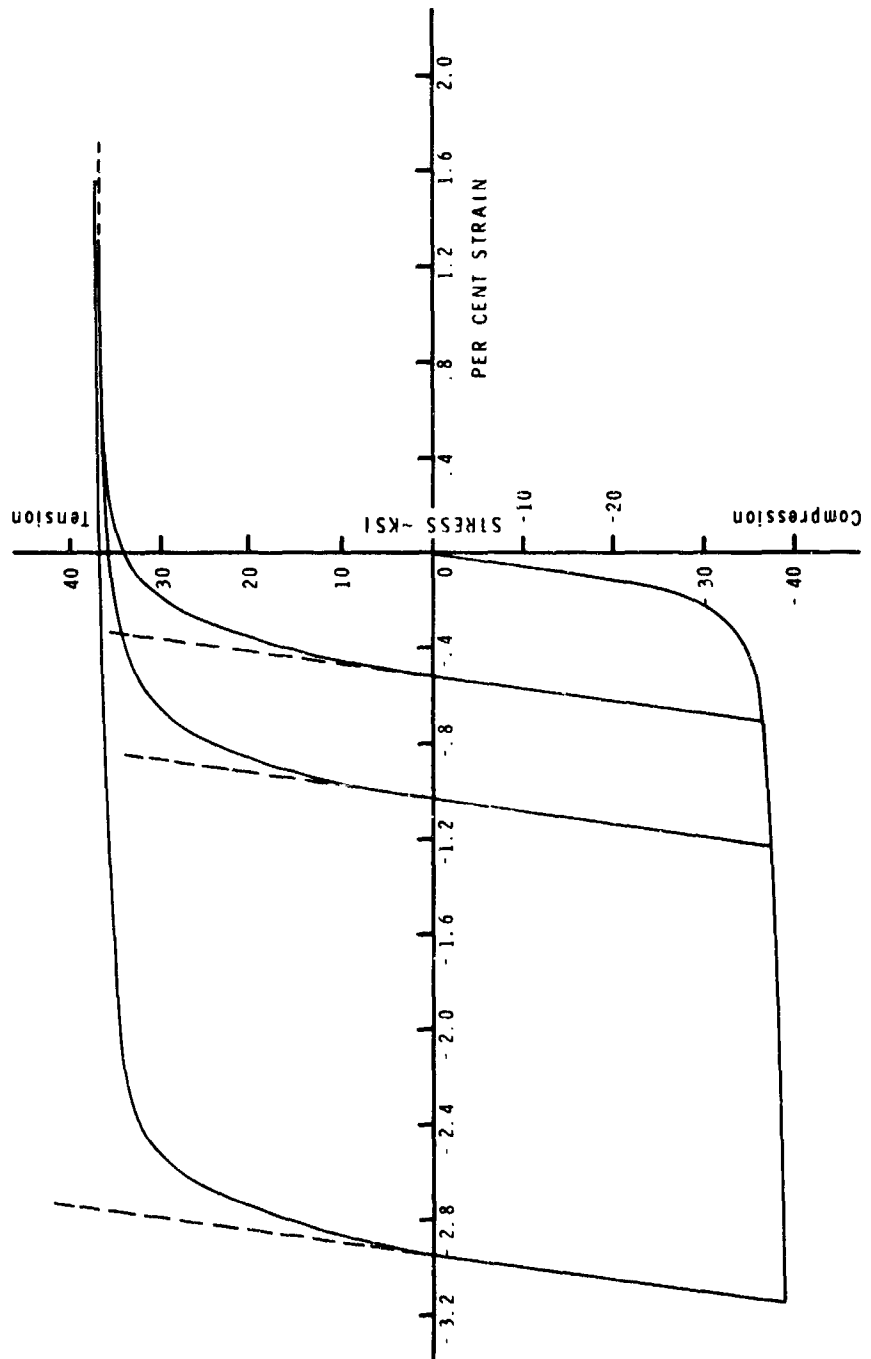


Figure 6 Reverse Loading Tests in Copper,
Strain Effects

The effect of additional strain limited cycles is shown in Figure 7 with the material work-softening as the number of previous loading cycles increases and approaching some equilibrium curve. This is similar to that seen by Morrow⁽¹⁰⁾ who found many materials tend to approach some saturated curve either by work-hardening or work-softening.

Although all of the present tests were performed at low strain rates (tests in the order of seconds) compared to those seen during shock wave loading, the data should give some indication of material behavior during reverse loading. The cross-effect (influence of unloading in some direction other than exactly opposite the loading path) was found important by Hecker⁽¹¹⁾ and others, but the present work describes the behavior on only one axis on the biaxial stress plane. For accuracy in material modeling, these effects should be considered if the material model must be used for a complex stress deformation.

Relating the reverse loading behavior to a dislocation mechanism is difficult in the uniaxial stress case and becomes more difficult as the stress state becomes more complex. Trying to relate the absolute magnitudes or Bauschinger strain to the microstructure of the material is impossible at this time and extrapolating the present data to materials having a microstructure different than the 1/2-hard OFHC copper tested would be unjustified.

MSL-70-23, Vol. V

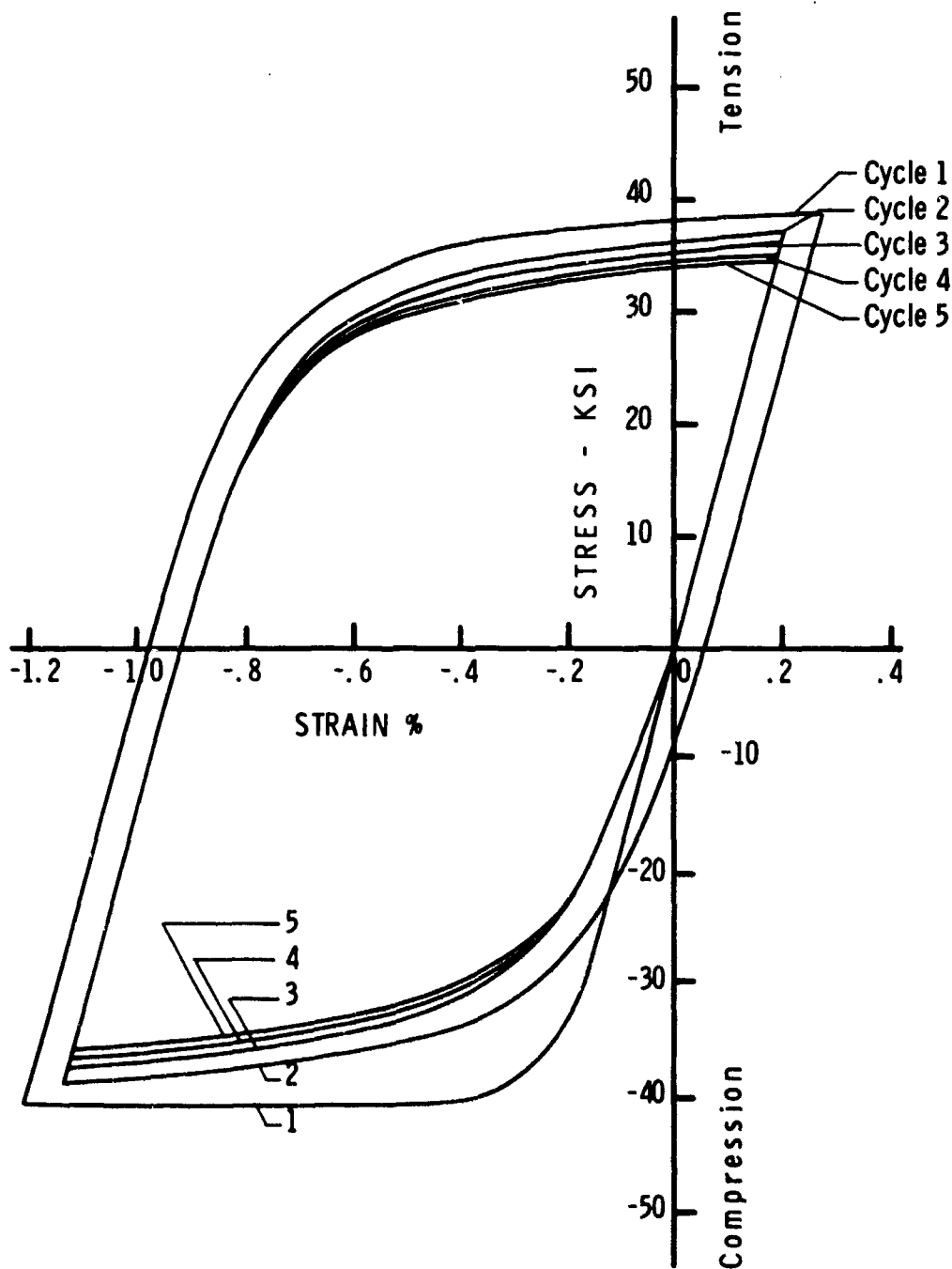


Figure 7 Reverse Loading Tests in Copper,
Cyclic Effects

SECTION III

ELASTIC BEHAVIOR

Measurement of elastic constants provides additional inputs to the study of material response. The three basic measurements are density, longitudinal (dilatational) wave velocity and shear (transverse) wave velocity. Values obtained at standard temperature and pressure (20°C and atmospheric pressure) establish the parameters used in first-order (temperature and pressure independent) calculations of material response. Measurements of temperature and pressure dependence permit more exact calculations to be made and, in particular, lead to prediction of pressure-compression isotherms, adiabats and hydrostats. If these measurements are made with sufficient accuracy (< 0.1%), the calculated pressure-compression behavior can frequently be extrapolated with reasonable confidence to higher pressures than covered in the actual measurements.

WAVE VELOCITY MEASUREMENTS

Initial measurements of longitudinal and shear wave velocities were made at 20°C and atmospheric pressure (i.e., $P = 0$). Values obtained were:

$$C_L = 4.757 \pm 0.004 \text{ mm/} \mu\text{sec}$$

$$C_S = 2.247 \pm 0.002 \text{ mm/} \mu\text{sec}$$

MSL-70-23, Vol. V

Measurements were then made of the temperature and hydrostatic pressure dependence of the wave velocities. Correction of the data for thermal expansion and hydrostatic compression gave the following:

Temperature Dependence, 0-100°C, $P = 0$

$$C_L = 4.766 - (0.000434 \times T) \text{ mm/} \mu\text{sec}$$

$$C_S = 2.253 - (0.000300 \times T) \text{ mm/} \mu\text{sec}$$

(T in °C)

Pressure Dependence, 0-9 kbar, $T = 20^\circ\text{C}$

$$C_L = 4.757 + (0.00685 \times P) \text{ mm/} \mu\text{sec}$$

$$C_S = 2.247 + (0.00243 \times P) \text{ mm/} \mu\text{sec}$$

(P in kbar)

Within the limits of experimental accuracy, the second-order coefficients were zero.

Third-order elastic constants can be determined by measuring elastic wave velocity as a function of uniaxial stress. A copper specimen was subjected to a static compressive load and C_L was measured normal to the loading direction. Over the stress range of 0 to 2 kbar, no change in C_L was observed (after correcting for lateral strain) within the accuracy of the measurements ($\pm 0.1\%$). The third-order elastic constants for copper single crystals have been reported by Salama and Alers⁽¹²⁾.

ELASTIC CONSTANTS

Assuming the material is isotropic* (C_L and C_S are independent of direction of measurement in a polycrystalline specimen), wave velocity data are used to calculate various elastic constants⁽¹⁴⁻¹⁶⁾. At 20°C and zero pressure, the following adiabatic constants were obtained (see Appendix A):

Longitudinal wave velocity, $C_L = 4.757 \text{ mm}/\mu\text{sec}$

Shear wave velocity, $C_S = 2.247 \text{ mm}/\mu\text{sec}$

Bulk wave velocity, $C_B = 3.99 \text{ mm}/\mu\text{sec}$

Sound wave velocity, $C_E = 3.70 \text{ mm}/\mu\text{sec}$

Rayleigh wave velocity, $C_R = 2.11 \text{ mm}/\mu\text{sec}$

Poisson's ratio, $\nu = 0.356$

Bulk modulus, $K = 1418 \text{ kbar}$

Shear modulus, $G = 450 \text{ kbar}$

Elastic modulus, $E = 1221 \text{ kbar}$

Lamé's parameter, $\lambda = 1117 \text{ kbar}$

The bulk and shear modulii are used in the development of the ultrasonic equation of state. They are obtained first as functions of T and P from the following:

$$K = \rho \left(C_L^2 - \frac{4}{3} C_S^2 \right) \quad (2)$$

$$G = \rho C_S^2 \quad (3)$$

* A cubic material is elastically isotropic when $\frac{2C_{44}}{C_{11}-C_{12}} = 1$,

where C_{44} , C_{11} and C_{12} are elastic stiffness constants.

Although single crystal copper is highly anisotropic with

$\frac{2C_{44}}{C_{11}-C_{12}} = \frac{2 \times 760}{1704-1226} = 3.2$ at 20°C⁽¹³⁾, this anisotropy may be

averaged out if the grains are randomly oriented crystallographically and the strain is uniform.

MSL-70-23, Vol. V

This gave:

Temperature dependence, $P = 0$

$$K_S = 1424 - (0.278 \times T) \text{ kbar}$$

$$G_S = 453 - (0.144 \times T) \text{ kbar}$$

Pressure dependence, $T = 20^\circ\text{C}$

$$K_S = 1418 + (5.53 \times P) \text{ kbar}$$

$$G_S = 450 + (1.30 \times P) \text{ kbar}$$

where the superscript S indicates adiabatic.

Finally, isothermal values of K and G as well as adiabatic and isothermal pressure and temperature derivatives at 20°C and zero pressure were calculated using the equations given in Appendix A. Results are given in Table I. Use of these constants in calculating the isotherm, adiabat and hydrostat is discussed in the section on Ultrasonic Equation of State.

GRUNEISEN PARAMETER⁽¹⁷⁾

The Gruneisen ratio γ is a parameter originally given by Gruneisen in a solid equation of state relating pressure to volume and energy ($\gamma = V (\partial P / \partial E)_V$). This parameter can be defined thermodynamically as:

$$\gamma = - \frac{1}{\rho c_p} \left(\frac{\partial V}{\partial T} \right)_P \left(\frac{\partial P}{\partial V} \right)_S = \frac{\beta K_S}{\rho c_p} \quad (4)$$

TABLE I

ELASTIC CONSTANTS FOR COPPER

(P = 0, T = 20°C)

PARAMETER	VALUE
K^S	1418 kbar
$(\frac{\partial K^S}{\partial P})_T = K_{0T}^{S'}$	5.53
$(\frac{\partial K^S}{\partial T})_P$	-0.278 kbar/°C
$(\frac{\partial K^S}{\partial P})_S = K_{0S}^{S'}$	5.40
$(\frac{\partial K^S}{\partial T})_S$	12.1 kbar/°C
K^T	1373 kbar
$(\frac{\partial K^T}{\partial P})_T = K_{0T}^{T'}$	5.59
$(\frac{\partial K^T}{\partial T})_P$	-0.408 kbar/°C
$(\frac{\partial K^T}{\partial P})_S = K_{0S}^{T'}$	5.42
$(\frac{\partial K^T}{\partial T})_S$	12.1 kbar/°C
$G^S = G^T$	450 kbar
$(\frac{\partial G}{\partial P})_T = G_{0T}^{'}$	1.30
$(\frac{\partial G}{\partial T})_P$	-0.144 kbar/°C
$(\frac{\partial G}{\partial P})_S = G_{0S}^{'}$	1.24
$(\frac{\partial G}{\partial T})_S$	2.76 kbar/°C

MSL-70-23, Vol. V

For an isotropic elastic solid, this can be expressed as

$$\gamma = \frac{\beta}{c_p} \left(c_L^2 - \frac{4}{3} c_S^2 \right) \quad (5)$$

where c_L and c_S are measured under adiabatic conditions.

At 20°C and zero pressure this gives

$$\gamma_0 = 2.13$$

The zero-pressure Gruneisen parameter can also be estimated by several other methods, including those of Slater⁽¹⁸⁾, Dugdale and MacDonald⁽¹⁹⁾, Anderson and Dienes^(20,21) and Schuele and Smith^(20,22). These methods are discussed in Appendix B.

An estimate of the temperature dependence of the Gruneisen parameter can be obtained by differentiating Equation 4 with respect to temperature. At constant pressure ($P = 0$, $T = 20^\circ\text{C}$):

$$\begin{aligned} \left(\frac{\partial \gamma}{\partial T} \right)_P &= \gamma_0 \left[\frac{1}{\beta} \left(\frac{\partial \beta}{\partial T} \right)_P + \frac{1}{K^S} \left(\frac{\partial K^S}{\partial T} \right)_P - \frac{1}{\rho} \left(\frac{\partial \rho}{\partial T} \right)_P \right. \\ &\quad \left. - \frac{1}{c_p} \left(\frac{\partial c_p}{\partial T} \right)_P \right] = -0.00076/\text{°C} \end{aligned} \quad (6)$$

The pressure dependence can be estimated by differentiating with respect to pressure (see Appendix C). At constant temperature ($T = 20^\circ\text{C}$, $P = 0$):

$$\left(\frac{\partial \gamma}{\partial P}\right)_T = \frac{\gamma_0}{K^S} \left[\left(\frac{\partial K^S}{\partial P}\right)_T + \frac{1}{\beta K^T} \left(\frac{\partial K^S}{\partial T}\right)_P - 1 \right. \\ \left. - \gamma - T \left(\frac{\partial \gamma}{\partial T}\right)_P \right] = -0.0020/\text{kbar} \quad (7)$$

Another approach is to assume γ/V constant, which permits $(\partial \gamma / \partial P)_T$ to be estimated directly from the bulk modulus data (see Appendix C). At constant temperature (20°C) :

$$\left(\frac{\partial \gamma}{\partial P}\right)_T = \frac{-\gamma_0}{\left(\frac{1}{K_0^T}\right)^{\left(1/K_0^{T'}\right)} \left(K_0^T + K_0^{T'}P\right)^{\left(1+K_0^{T'}\right)/K_0^{T'}}} \\ = \frac{-7.76}{(1373 + 5.59P)^{1.178}} \\ = -0.0016/\text{kbar} @ P = 0 \\ = -0.0010/\text{kbar} @ P = 100 \text{ kbar} \quad (8)$$

McQueen and Marsh⁽²³⁾ used shock velocity data to calculate γ (assuming $\gamma = f(V)$), which gave $\Delta \gamma / \Delta P \approx -0.002$ at $P = 0$ and $\Delta \gamma / \Delta P \approx -0.001$ at $P = 100$ kbar.

DEBYE TEMPERATURE^(24,25)

The Debye temperature θ is a parameter related to the maximum number of oscillation frequencies a system assumed to be an

MSL-70-23, Vol. V

elastic continuum can support. It is an important parameter in thermal energy calculations and indicates the temperature above which variations due to temperature for some thermodynamic parameters such as specific heat, thermal expansion and Gruneisen ratio become small. There are a number of methods for calculating the Debye temperature, and one approximation suitable for use with elastic wave velocity data for polycrystalline metals is:

$$\theta = \frac{h}{k} \left(\frac{9N}{4\pi V} \right)^{1/3} \left(\frac{1}{C_L^3} + \frac{2}{C_S^3} \right)^{-1/3}$$

where h is Planck's constant, k is Boltzmann's constant, N is number of mass points and V is sample volume.

At 20°C, the elastically-determined Debye temperature for copper is:

$$\theta = 4.3 \times 10^{-5} \left(\frac{N}{V} \right)^{1/3} \left(\frac{1}{C_L^3} + \frac{2}{C_S^3} \right)^{-1/3} \quad (9)$$

$$\theta = 331^\circ\text{K}$$

for $N = 4$ (atoms per unit cell), $V = (3.615 \times 10^{-7} \text{ mm})^3$ (lattice constant), $C_L = 4.757 \text{ mm}/\mu\text{sec}$ and $C_S = 2.247 \text{ mm}/\mu\text{sec}$.

This compares well with the value $\theta = 331.3^\circ\text{K}$ obtained by a more exact computer method using single-crystal elastic data. (25)

SECTION IV

EQUATION OF STATE

The development of material response models and computational codes requires extensive data on material behavior under uniaxial strain conditions, including equation of state, wave propagation and spall fracture. Most data are used directly in developing models of material behavior, although independent check data (attenuated wave shapes and spall wave profiles) are necessary to determine accuracy of the calculations. This section presents the equation of state analysis, and the following two sections cover wave propagation and spall fracture.

SHOCK WAVE EQUATION OF STATE

The hugoniot equation of state is the locus of equilibrium states reached after shocking of a material, and the data are usually obtained either as stress-particle velocity points or as shock velocity-particle velocity points. The shock wave hugoniot data for copper presented in this report were obtained with x-cut quartz gages and optical techniques. Representative quartz gage records for direct impact and transmitted wave tests are shown in Figure 8. The buffered direct impact method (tungsten carbide buffer plate on front of the quartz) permitted stresses up to 80 kbar in the copper while keeping the stress in the quartz at an acceptable level. The use of quartz gages for transmitted wave tests was primarily for the study of compressive wave development and elastic precursor decay and results are discussed in the Wave Propagation section. The direct

MSL-70-23, Vol. V

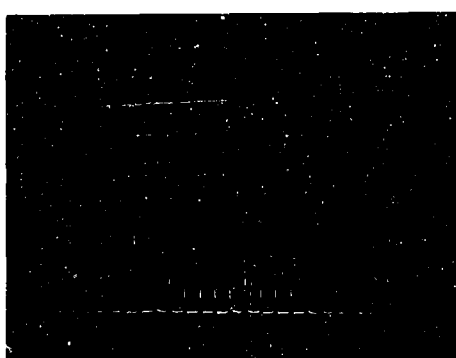


DIRECT IMPACT

$\text{Cu} \rightarrow \text{Q}$

$V_I = 0.0906 \text{ mm}/\mu\text{s}$

$\sigma_H = 9.9 \text{ kbar}$



DIRECT IMPACT, BUFFERED

$\text{Cu} \rightarrow \text{WC}/\text{Q}$

$V_I = 0.159 \text{ mm}/\mu\text{s}$

$\sigma_H = 44.0 \text{ kbar}$



TRANSMITTED WAVE

$\text{Al} \rightarrow \text{Cu}/\text{Q}$

$V_I = 0.165 \text{ mm}/\mu\text{s}$

$\sigma_H = 18.1 \text{ kbar}$

Figure 8 Quartz Gage Records

impact records, which give a stress-particle velocity point since the hugoniot of quartz is known, showed very fast rise times (< 10 nsec) and then a constant peak stress for the duration of the gage transit time. The slight rounding at the front of the direct impact records in Figure 8 is due to impact tilt, and the ramped peak stress region results from finite-strain effects in the quartz which are corrected in the data analysis.

Hugoniot data at stresses of 100 to 200 kbar were obtained by using a streak camera and a target in the form of a two-step cylinder ("hat" configuration). A schematic of the technique and a sample record are shown in Figure 9. The two surfaces of the target are viewed through the camera slit and shock arrival is observed as a change in surface reflectance. The average shock velocity is obtained from the record, and particle velocity is assumed to be $1/2 V_I$ (impact velocity) since impactor and target are the same material.

The hugoniot may be expressed in several forms. A convenient form for experimental work is the hugoniot centered about zero stress and particle velocity, as established by a least-squares fit to the data in the stress-particle velocity ($\sigma_H - u_p$) plane. Transformation of the hugoniot into various planes, such as shock velocity-particle velocity ($U_S - u_p$) and stress-volume ($\sigma_H - v$), is performed by assuming a material model. This was done by assuming an ideal elastic-plastic wave structure with equilibrium initial and final states and applying the mass and momentum conservation equations. This leads to:

$$\sigma_H = \sigma_e + \rho_e (U_S - u_e) (u_p - u_e) \quad (10)$$

MSL-70-23, Vol. V

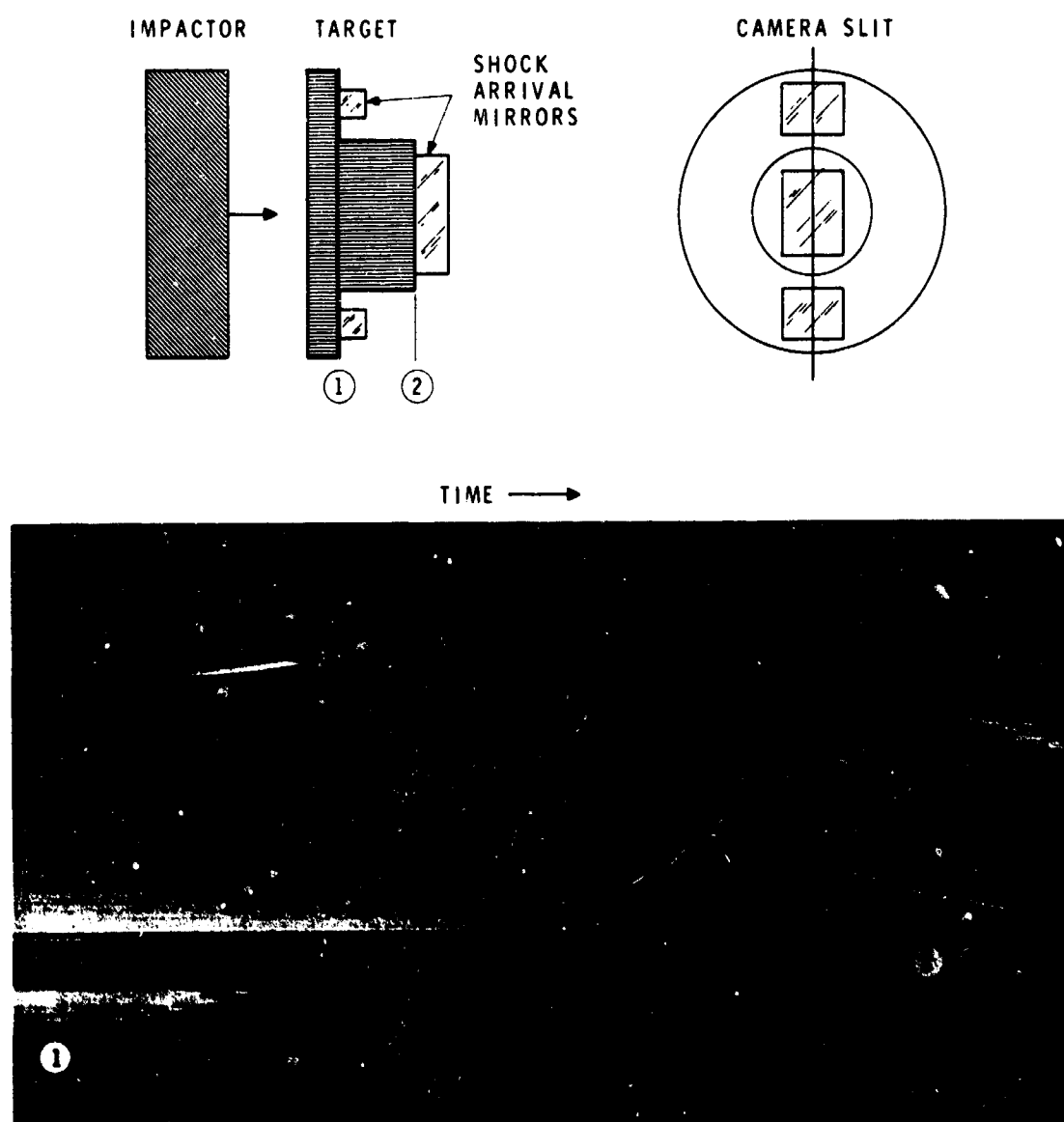


Figure 9 Streak Camera Record, "Hat" Target

and

$$v = v_o \left(1 - \frac{u_e}{c_L} \right) \left(\frac{u_s - u_p}{u_s - u_e} \right) \quad (11)$$

where ρ_e and u_e are density and particle velocity at the elastic limit σ_e .

Therefore, when either $\sigma_H - u_p$ or $u_s - u_p$ relations are established and σ_e , ρ_e , u_e and c_L are known, σ_H , u_s , u_p and v are uniquely determined. The resulting equations of state for copper are given in Figures 10, 11 and 12 and are listed below:

$$\left. \begin{aligned} \sigma_H &= 1.5 + 344 u_p + 143 u_p^2 \quad (\text{Std. Error}=0.4 \text{ kbar}) \\ \sigma_H &= 3.1 + 1308 \mu + 3520 \mu^2 \\ P_H &= 1308 \mu + 3520 \mu^2 \quad (\text{Hydrostat}) \\ u_s &= 3.915 + 1.53 u_p \end{aligned} \right\} \quad (12)$$

where $\mu = (v_o/v) - 1$

These equations of state are based on the measurements indicated by the symbols in Figure 10 and $\sigma_e = 8$ kbar, and are considered to be valid over the stress range of 10 to 200 kbar. Accuracy of the data points are estimated to be $\pm 2\%$ for σ_H and $\pm 1\%$ for u_p .

The hydrostat ($P_H - \mu$) was obtained by subtracting the stress-axis intercept value from the $\sigma_H - \mu$ equation. This approach

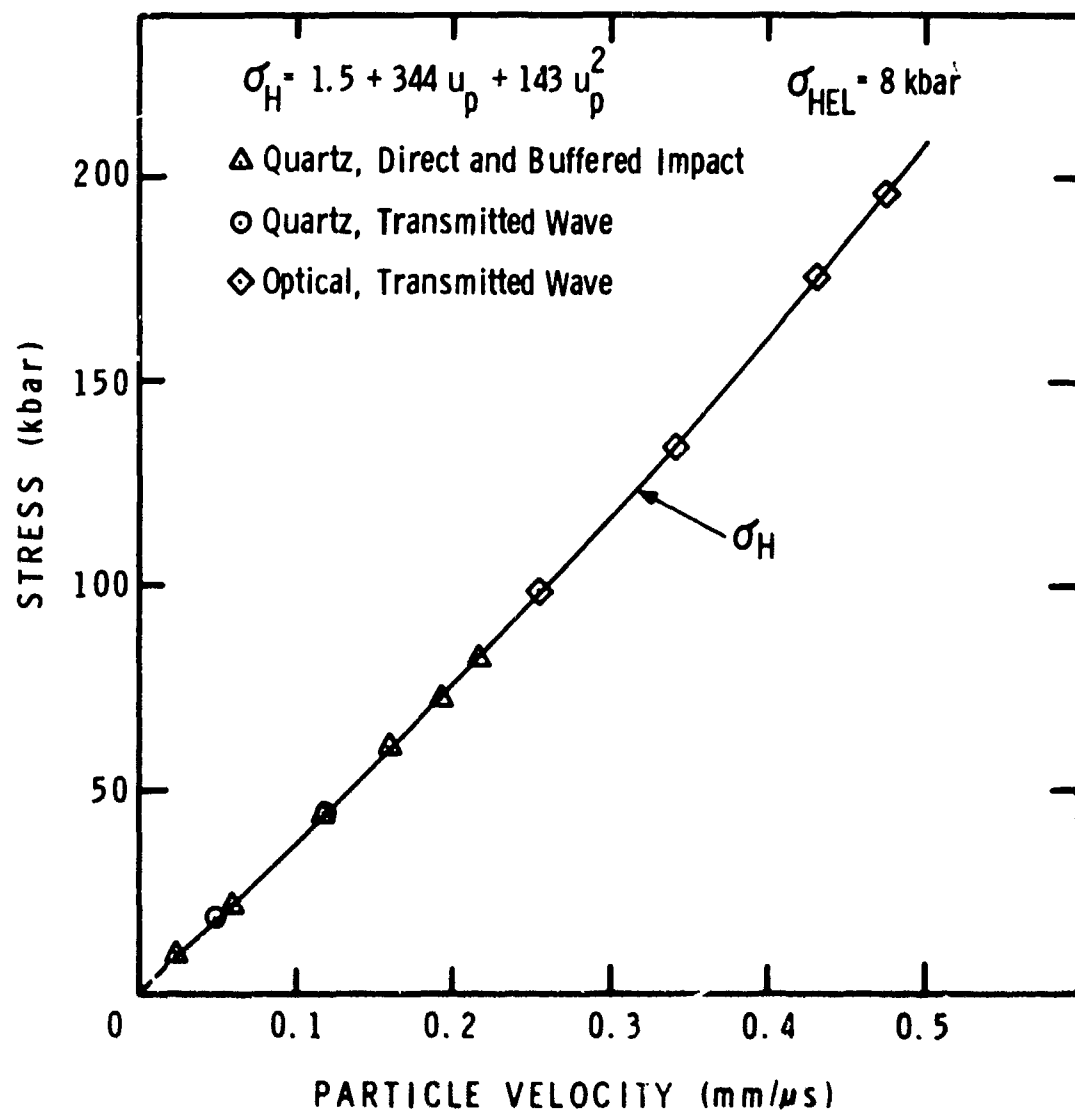


Figure 10 Stress-Particle Velocity Hugoniot, Copper

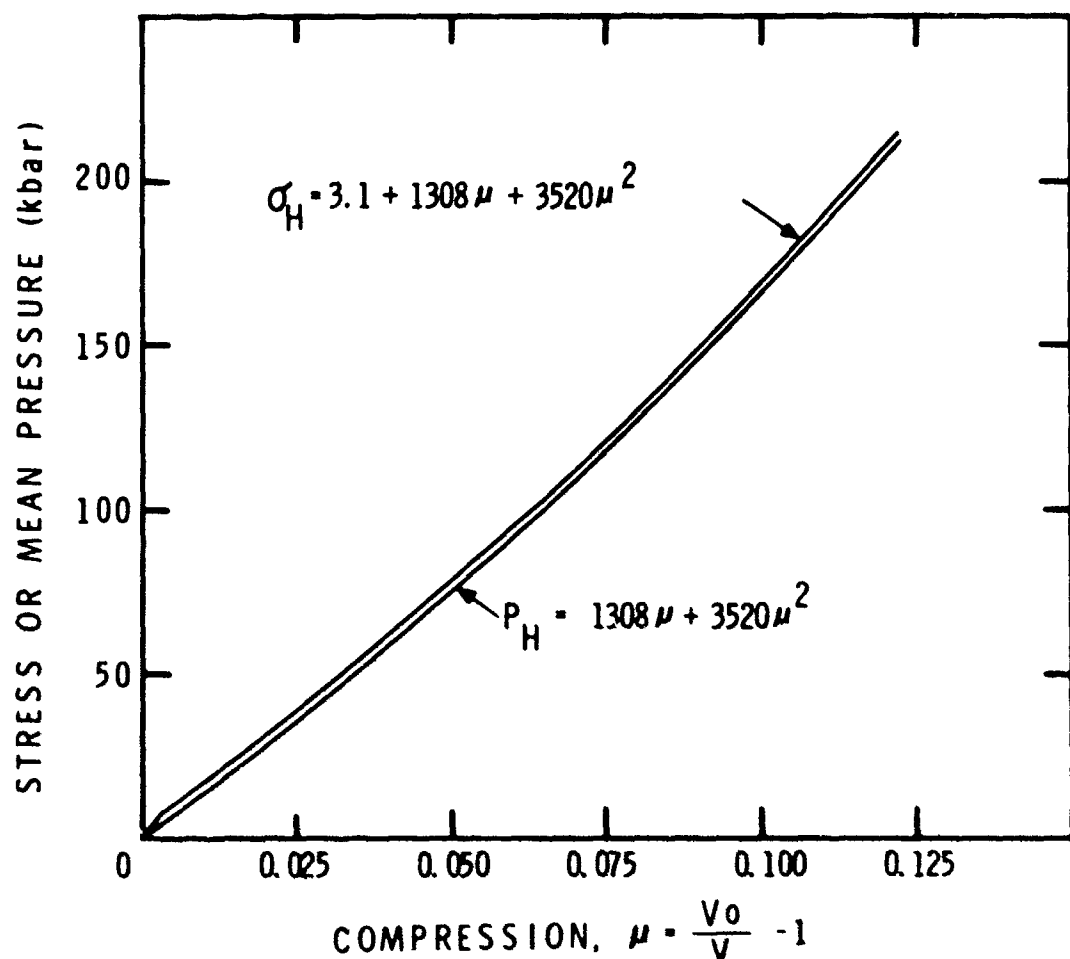


Figure 11 Stress or Mean Pressure - Compression
Hugoniot, Copper

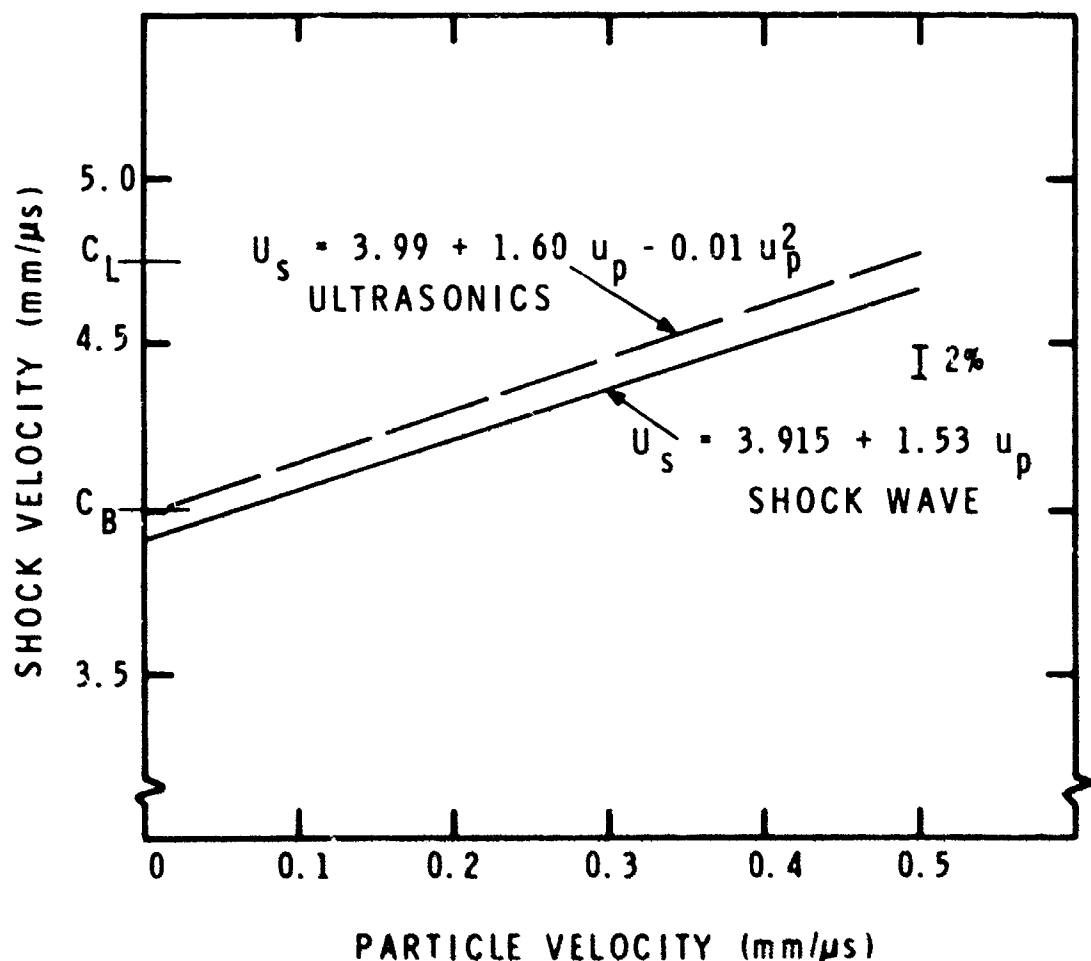


Figure 12 Shock Velocity-Particle Velocity Hugoniot, Copper

satisfies the requirement that the $P_H - \mu$ function pass through the origin, assumes the deviatoric stress (σ_D) is constant (no strain hardening), and implies a value of 3.1 kbar for σ_D . Alternative ways of estimating σ_D are discussed in Appendix D.

The low-pressure hugoniot of copper (99.95%) has been reported previously by Munson and Barker,⁽²⁶⁾ who used the flat-plate impact technique and free surface velocity measurements to determine the hugoniot up to 116 kbar. They calculated the hydrostat (hugoniot mean pressure), adiabat and isotherm, using corrections for the deviatoric stress, entropy change and temperature change. The hydrostat was given as:

$$\frac{\mu}{1+\mu} = 0.734 \times 10^{-3} P_H - 1.41 \times 10^{-6} P_H^2 \quad (13)$$

Comparing this with the hydrostat obtained in the present study gives:

μ	P_H (Eq. 12) kbar	P_H (Eq. 13) kbar
0.020	27.6	28.2
0.040	58.0	59.1
0.060	91.2	94.1

The agreement is reasonable below 100 kbars.

The high-pressure hugoniot of copper was recently reported by Isbell, et al.,⁽²⁷⁾ as:

$$u_s = 3.964 + 1.463 u_p \quad (14)$$

MSL-70-23, Vol. V

This relation is based on shock velocity-particle velocity measurements over the range of 1 to 5 mbar.

ULTRASONIC EQUATIONS OF STATE

The equation of state can also be determined from ultrasonics measurements (see, e.g., Ref. 28 to 31). The very accurate measurement of elastic wave velocities (and, therefore, bulk modulus) as a function of hydrostatic pressure makes it possible to directly estimate shock wave compression behavior. To combine the ultrasonics data with shock wave data to predict very high pressure response. Numerous analytical and empirical relations have been developed for relating pressure, volume and bulk modulus, including those Birch, (32,33) Murnaghan (34) and Keane (35,36). The use of these relations is discussed in Appendix E and the results are summarized below:

Birch EOS

$$P_T = 2060 \left[\left(1+\mu \right)^{7/3} - \left(1+\mu \right)^{5/3} \right] \left[1+1.19 \left\{ \left(1+\mu \right)^{2/3} - 1 \right\} \right] \quad (15)$$

Murnaghan EOS, Isotherm

$$P_T = 245.6 \left[\left(1+\mu \right)^{5.59} - 1 \right] \quad (16)$$

Murnaghan EOS, Adiabat

$$P_S = 262.6 \left[\left(1+\mu \right)^{5.40} - 1 \right] \quad (17)$$

Keane EOS, $K_{\infty}^{S'}$ = 3.7

$$P_S = 559.3 \left[\left(1+\mu \right)^{3.7} - 1 \right] - 651.5 \ln \left(1+\mu \right) \quad (18)$$

Keane EOS, $K_{\infty}^{S'}$ = 2.73

~~$$P_S = 1025 \left[\left(1+\mu \right)^{2.73} - 1 \right] - 1383 \ln \left(1+\mu \right) \quad (19)$$~~

In the above equations, subscripts T and S indicate isothermal and isentropic, respectively.

Duvall gives a correction for the change in entropy across a shock front based on the Murnaghan equation of state: (30,37)

$$P_H = P_S + \frac{\gamma_0 K_0^S}{12} \left(K_{0S}^{S'} + 1 \right) \left(\frac{\mu}{1+\mu} \right)^3$$

$$P_H = P_S + 1611 \left(\frac{\mu}{1+\mu} \right)^3 \quad (20)$$

Zel'dovich gives an expression relating P_S and P_T , assuming γ/v is constant: (30,38)

$$P_S = P_T + \beta T_0 K_0^T \left[\exp \left\{ \gamma_0 \left(\frac{\mu}{1+\mu} \right) \right\} - \left(1+\mu \right) \right]$$

$$P_S = P_T + 20.8 \left[\exp \left\{ 2.13 \left(\frac{\mu}{1+\mu} \right) \right\} - \left(1+\mu \right) \right] \quad (21)$$

The above equations of state are compared to the shock wave EOS in Table II. The entropy correction based on the Murnaghan equation has been applied to the Birch and Keane equations as well. The ultrasonic equations of state show good agreement with each other but all give mean pressure values at a given compression that are 4-8% higher than the shock wave hydrostat, up to 250 kbars.

The shock velocity-particle velocity relationship can also be determined from ultrasonic data. Following the method of Ruoff⁽³⁹⁾ one obtains:

$$u_s = C_B + S u_p + A u_p^2 \quad (22)$$

$$\text{where } C_B = \left(\frac{K_0^S}{10\rho_0} \right)^{1/2}$$

$$S = 1/4 \left(K_{0S}^{S'} + 1 \right)$$

$$A = \frac{1}{24 C_B} \left[S \left(7 - K_{0S}^{S'} + 4\gamma_0 \right) + 2K_0^S K_{0S}^{S''} \right] \quad \left. \right\} (23)$$

For copper:

$$u_s = 3.99 + 1.60 u_p + 0.17 u_p^2$$

The u_p^2 coefficient (0.17) was calculated assuming $K_{0S}^{S''} = 0$. A positive second-order coefficient implies a concave upward $u_s - u_p$ curve. However, comparison of low-pressure (Eq. 12) and high-pressure (Eq. 14) shock wave data indicates that the slope of the $u_s - u_p$ curve decreases slightly with increasing

TABLE II
EQUATIONS OF STATE COMPARISON-HYDROSTAT

$\mu = \frac{V_0}{V} - 1$	P _H , HUGONIOT MEAN PRESSURE (kbar)						
	BIRCH EQ. 15		MURNAGHAN EQ. 16		KEANE EQ. 18 EQ. 19		SHOCK WAVE EQ. 12
0.025	36.9	37.4	37.4	37.4	37.4 37.3	34.9	
0.050	78.2	79.4	79.3	79.1	78.8	74.2	
0.075	123.8	126.3	126.0	125.0	124.4	117.9	
0.100	174.4	178.4	177.9	175.6	175.3	166.0	
0.125	229.9	236.5	235.6	231.0	228.4	218.5	

MSL-70-23, Vol. V

pressure.* If one assumes that the relation given above for 'A' is valid then K_{OS}^S can be estimated as a function of 'A'. For example, for a linear $U_S - u_p$ relation, $A = 0$ and $K_{OS}^S = -0.0057$. Pastine and Piacesi⁽⁴⁰⁾ calculated $A = 0.0144$ (using data of McQueen and Marsh⁽²³⁾) which gives $K_{OS}^S = -0.0062$. It would seem that $K_{OS}^S \approx -0.006$ for copper at zero pressure, which gives the following as a more reasonable ultrasonic $U_S - u_p$ relation for low pressures:

$$U_S = 3.99 + 1.60 u_p - 0.01 u_p^2 \quad (24)$$

This is compared with the linear $U_S - u_p$ relation obtained from low-pressure shock wave data in Figure 12.

YIELD BEHAVIOR

A complete description of the low-pressure equation of state requires consideration of yield behavior or the hugoniot elastic limit. Values of compressive yield were obtained by three independent methods.

A. Uniaxial Stress

The yield level was determined in uniaxial stress (σ_e) as a function of strain rate and then converted to uniaxial strain using:

$$\sigma_e = \sigma_0 \left(\frac{1-v}{1-2v} \right) \quad (25)$$

* This comparison assumes no phase change and no melting.

Strain Rate <u>sec⁻¹</u>	σ_e <u>kbar</u>
10^3	7.0
10^{-3}	5.8

B. Wave Profiles

The elastic precursor level was measured as a function of propagation distance using quartz gages. These profiles are discussed in the section on Wave Propagation.

Propagation Distance <u>mm</u>	σ_e <u>kbar</u>
2	~4.0
12	~2.8

C. Hugoniots

The yield level in uniaxial strain was inferred by comparison of the elastic ($\rho_0 C_L$) and plastic (σ_H vs. u_p) hugoniots, i.e., by defining the elastic limit as the intersection of the elastic response line and the curve-fit to the stress-particle velocity data:

$$10 \rho_0 C_L u_e = A + B u_e + C u_e^2$$

solve for u_e

$$\text{then } \sigma_e = 10 \rho_0 C_L u_e$$

MSL-70-23, Vol. V

$$u_e = 0.019 \text{ mm}/\mu\text{s}$$

$$\sigma_e = 8.0 \text{ kbar}$$

For an isotropic, polycrystalline metal with elastic-perfectly plastic behavior and no strain-rate or time-dependent effects, one would expect the same yield level to be obtained by each method. However, copper shows both strain-rate sensitivity and decay of the elastic precursor. Also, the elastic wave is not well-defined and shows spreading (increasing rise time) as well as decay with distance. Because of these effects, the elastic limit is not single-valued and a compromise must be made in selecting a value for use in the hugoniot transformation equations given earlier where elastic-perfectly plastic behavior was assumed.

The elastic limit calculated from the hugoniots (8 kbar) was used in determining the $\sigma_H - \mu$ and $U_S - u_p$ equations given for copper in the low-pressure region. Extrapolation of the uniaxial stress tests to $\sim 10^5/\text{sec}$ would give an equivalent yield in uniaxial strain of $\sim 8 \text{ kbar}$. Although this extrapolation is very uncertain, the strain rate in the elastic wave front in copper is about 10^5 to $10^6/\text{sec}$. Therefore, the use of 8 kbar as the hugoniot elastic limit is consistent with the uniaxial stress measurements. The yield as determined from the wave profiles, however, is considerably lower than 8 kbar, at least for propagation distances greater than 2 mm. Also, the precursor amplitude attenuates $> 80\%$ in copper in the first 2 mm, which is much higher than observed for other metals. The reasons for this apparent disagreement are not known, but may be related to some microscale metallurgical factor such as microyielding or to the elastic anisotropy of single crystal copper.

METALLOGRAPHIC STUDIES

Grain structure in copper subjected to shock loading is shown in Figure 13. Compressive pulse duration for these tests was $\sim 1\mu\text{sec}$. There is some evidence of macrotwinning although it has affected a relatively small volume and did not increase appreciably from 18 to 86 kbar, and the increase in hardness was small (~ 78 to $84 R_F$). Smith⁽⁴¹⁾ found the macrotwin density to still be low at 225 kbar but to become substantial at 425 kbar. It is unlikely that the elastic wave behavior in copper can be attributed to the effects of macrotwin formation, especially when there is evidence that the twinning may occur during the release portion of the compressive pulse.^(41,42)

Shock-loaded copper also shows twinning on a microscale, i.e., twins on the order of $0.5 \mu\text{m}$ width which are too small to be seen optically. Examples from transmission electron microscope of shock-loaded copper foil (not in the same initial condition as the bar stock) are shown in Figure 14. The dislocation density in the as-received foil was estimated at $\sim 10^{10}/\text{cm}^2$ with a few microtwins observable, while the shocked (34 kbar, $0.5 \mu\text{sec}$ pulse) foil appeared to have a higher dislocation density with definite indication of increased microtwinning. Transmission electron microscope studies by other investigators (see e.g., Refs. 42 to 46) have indicated that microtwinning may occur at stresses as low as 16 kbars, and becomes substantial in the range of 100 to 200 kbars. These studies also showed substantial dislocation cell structure development with dislocation densities on the order of $10^{11}/\text{cm}^2$ for stress levels of several hundred kbars.

MSL-70-23, Vol. V

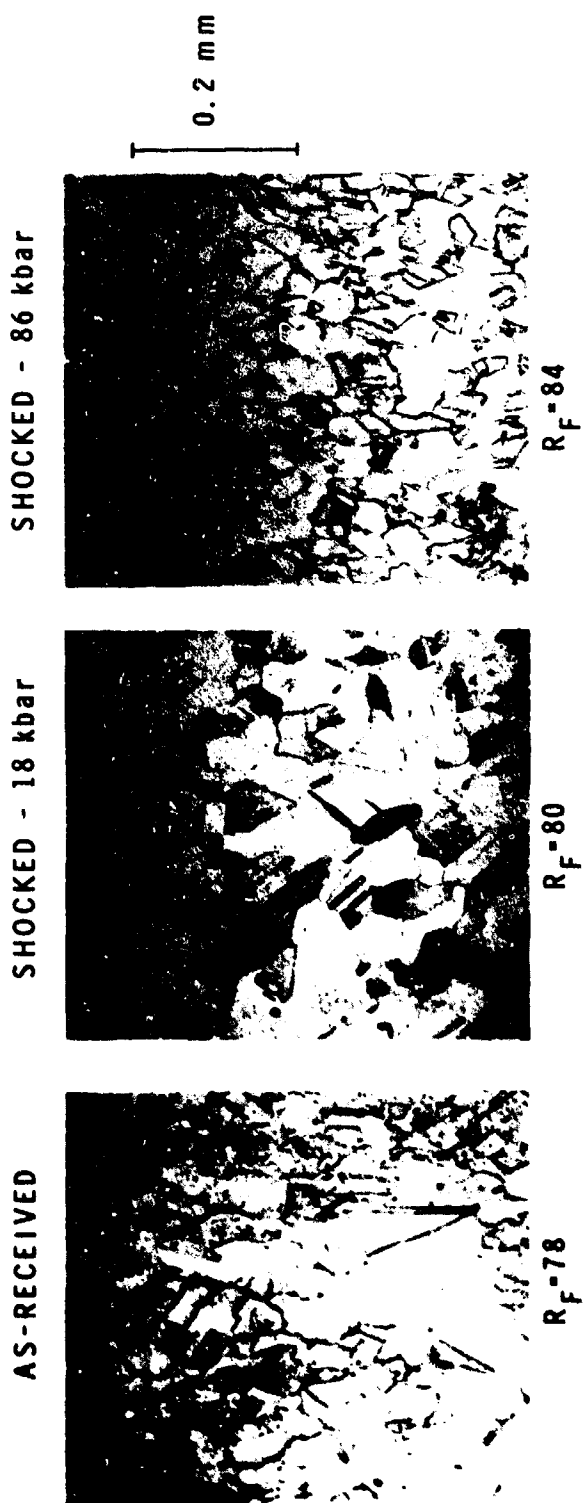


Figure 13 Shock Wave Test Specimens, Copper

METALLOGRAPHIC STUDIES

Grain structure in copper subjected to shock loading is shown in Figure 13. Compressive pulse duration for these tests was $\sim 1\mu\text{sec}$. There is some evidence of macrotwinning although it has affected a relatively small volume and did not increase appreciably from 18 to 86 kbar, and the increase in hardness was small (~ 78 to $84 R_F$). Smith⁽⁴¹⁾ found the macrotwin density to still be low at 225 kbar but to become substantial at 425 kbar. It is unlikely that the elastic wave behavior in copper can be attributed to the effects of macrotwin formation, especially when there is evidence that the twinning may occur (41,42) during the release portion of the compressive pulse.

Shock-loaded copper also shows twinning on a microscale, i.e., twins on the order of $0.5\ \mu\text{m}$ width which are too small to be seen optically. Examples from transmission electron microscope of shock-loaded copper foil (not in the same initial condition as the bar stock) are shown in Figure 14. The dislocation density in the as-received foil was estimated at $\sim 10^{10}/\text{cm}^2$ with a few microtwins observable, while the shocked (34 kbar, $0.5\ \mu\text{sec}$ pulse, foil appeared to have a higher dislocation density with definite indication of increased microtwinning. Transmission electron microscope studies by other investigators (see e.g., Refs. 42 to 46) have indicated that microtwinning may occur at stresses as low as 16 kbars, and becomes substantial in the range of 100 to 200 kbars. These studies also showed substantial dislocation cell structure development with dislocation densities on the order of $10^{11}/\text{cm}^2$ for stress levels of several hundred kbars.

MSI-70-23, Vol. V

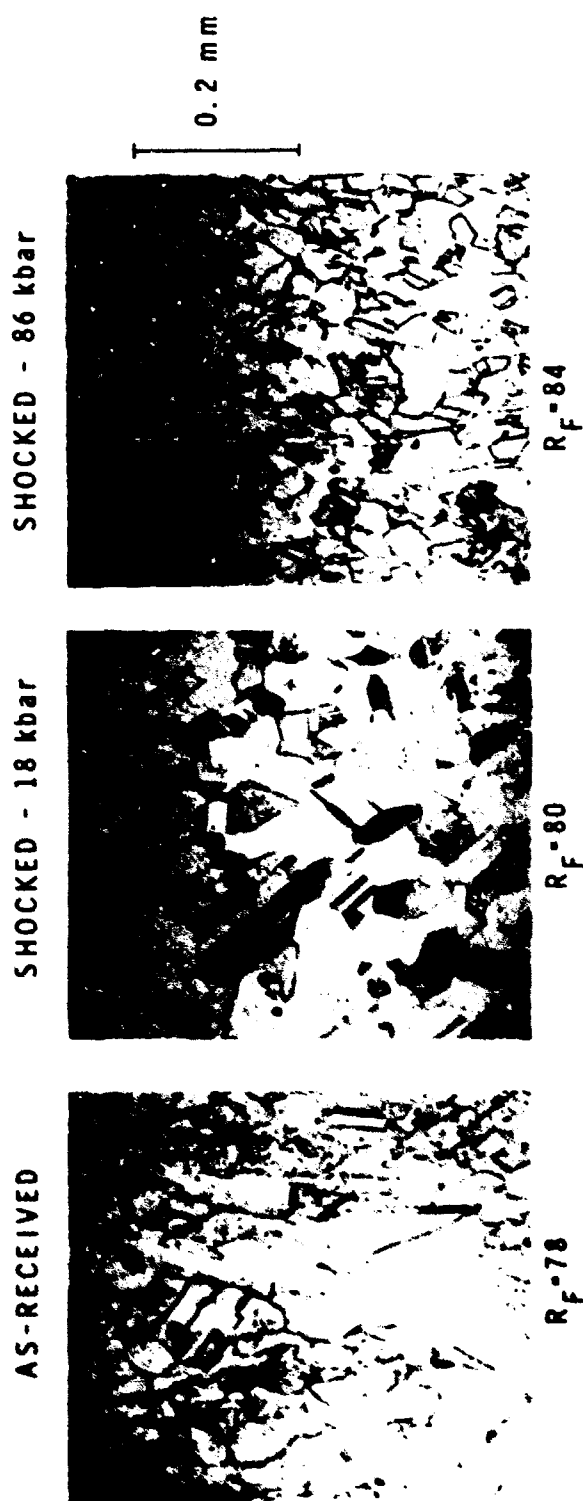


Figure 13 Shock Wave Test Specimens, Copper

AS-RECEIVED



SHOCK-LOADED-34 kbar



Figure 14 As-Received and Shock-Loaded Copper Poils, Transmission Electron Micrographs

MSL-70-23, Vol. V

SECTION V

WAVE PROPAGATION

Compressive wave development and elastic precursor decay are used as basic input data for material response models, while a complete understanding of shock wave propagation requires inclusion of release wave behavior. Wave attenuation data provide the most stringent check on the accuracy of shock wave response calculations.

COMPRESSIVE WAVE BEHAVIOR

Profiles of shock waves propagated through a specimen are obtained as stress-time or velocity-time histories. Profiles may be used in this form directly for comparison with calculated or predicted material response. When it is necessary to transform the data to obtain material stress from transducer stress or particle velocity from interface velocity, an impedance matching technique is applied, utilizing the conservation relations and assuming time-independent behavior. The implications of this assumption must be considered when utilizing the transformed data.

Structure in the compressive wave front in copper is shown in the quartz gage data in Figure 15.* The wave front is characterized by a non-steady-state elastic portion and a transition to a spreading plastic wave (nominal final stress of 18 kbar). The elastic wave would be overdriven by the plastic wave at ~ 200 kbar.

* In this and subsequent figures containing quartz gage data, tilt refers to the time required for a step-input to sweep across the gage electrode diameter.

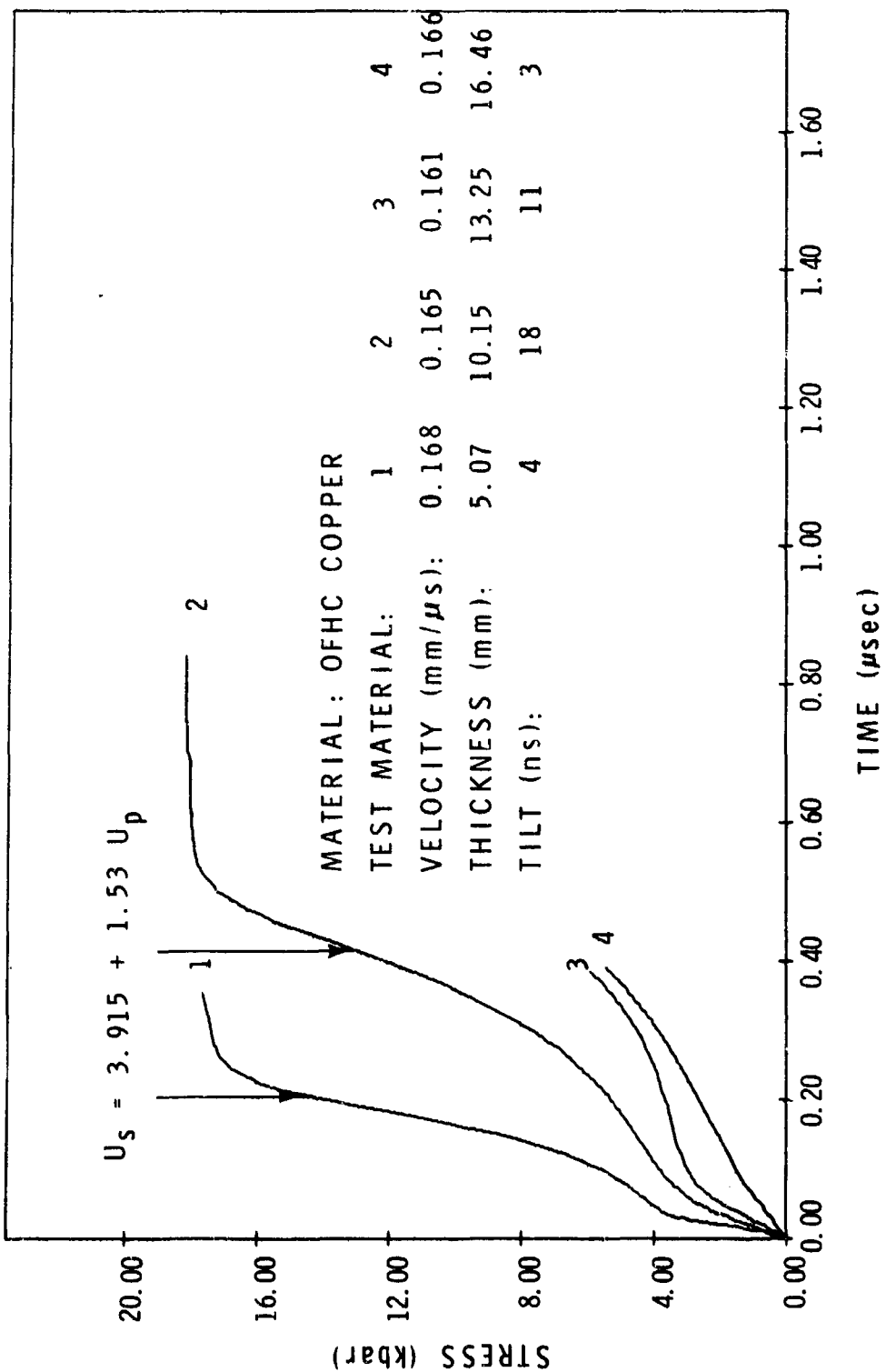


Figure 15 Compressive Waves, Propagation Distance

MSL-70-23, Vol. V

The rise-time of the elastic wave is too large to be attributed to tilt effects. It seems evident that only the initial elastic disturbance is traveling with longitudinal wave velocity (C_L), and subsequent stress increments in the elastic wave are traveling with lower velocity. This behavior is not appreciably influenced by peak stress, as shown in Figure 16. The front portion of the waves overlap almost exactly for peak stresses of 18 and 44 kbar. Compressive waves in 1/2-hard and annealed copper are compared in Figure 17. The elastic portion has almost disappeared for the annealed material (see Figure 2 for micro-structure). These profiles indicate that wave structure is very sensitive to thermal-mechanical history of the specimen.

Although the conditions for development of steady-state plastic waves in copper were not studied in detail (i.e., the minimum propagation distance for a given stress level at which the plastic wave rise-time becomes constant was not established), the rise-time in the plastic wave increases as propagation distance goes from 5 to 10 mm at 18 kbar (see Figure 15). Also shown in Figures 15 and 16 are the shock wave velocities as calculated from the shock wave hugoniot (Equation 12). Although there is qualitative agreement in that the predicted plastic wave velocity lies within the rise-time of the measured wave, the plastic wave cannot be considered to have a unique velocity for a given stress level, at least for stresses below ~ 50 kbar. This means that transformation of the hugoniot from the $\sigma_H - u_p$ plane to $\sigma_H - \mu$ or $U_S - u_p$ by assuming ideal elastic-plastic wave structure and steady-state conditions can lead to considerable uncertainty at lower stresses.

Elastic precursor structure in copper has also been studied by Jones and Mote⁽⁴⁷⁾ using flat-plate impact techniques and quartz gages. For annealed single crystals, they found elastic

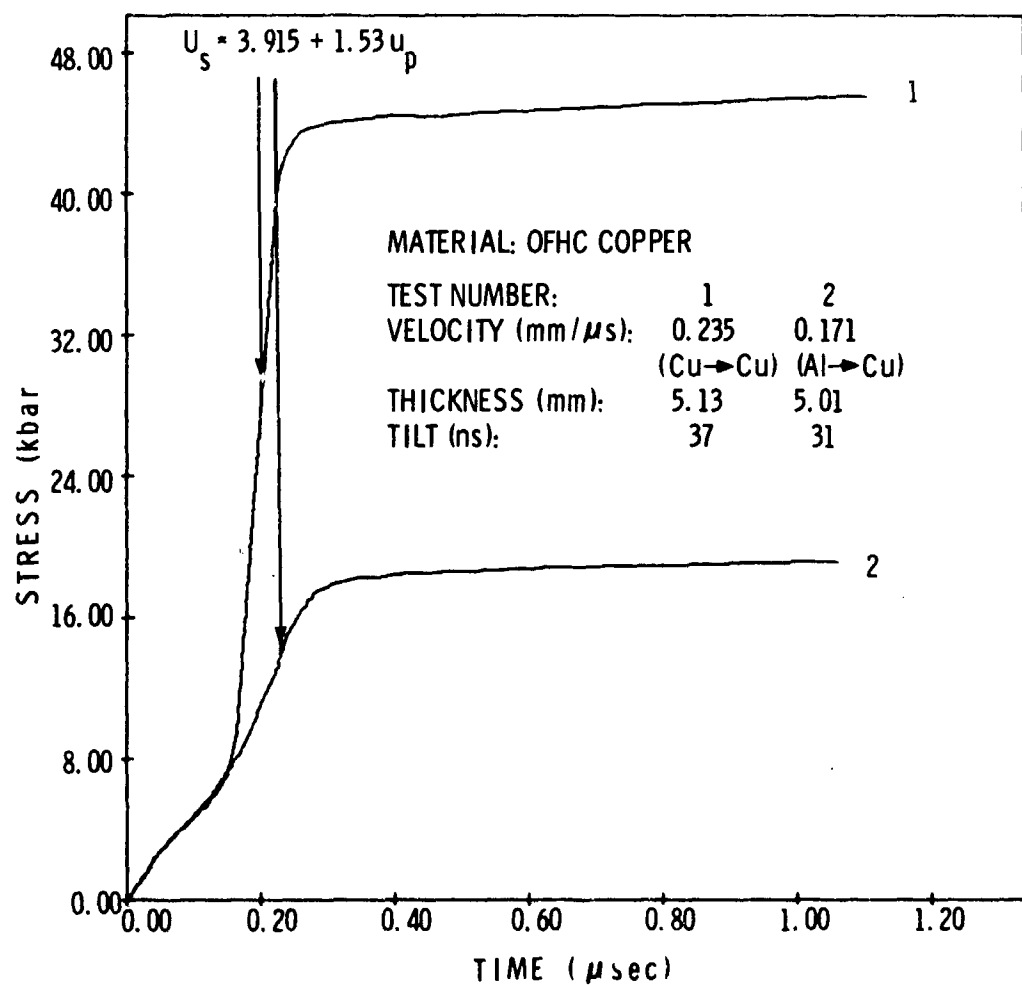


Figure 16 Compressive Waves, Peak Stress Dependence

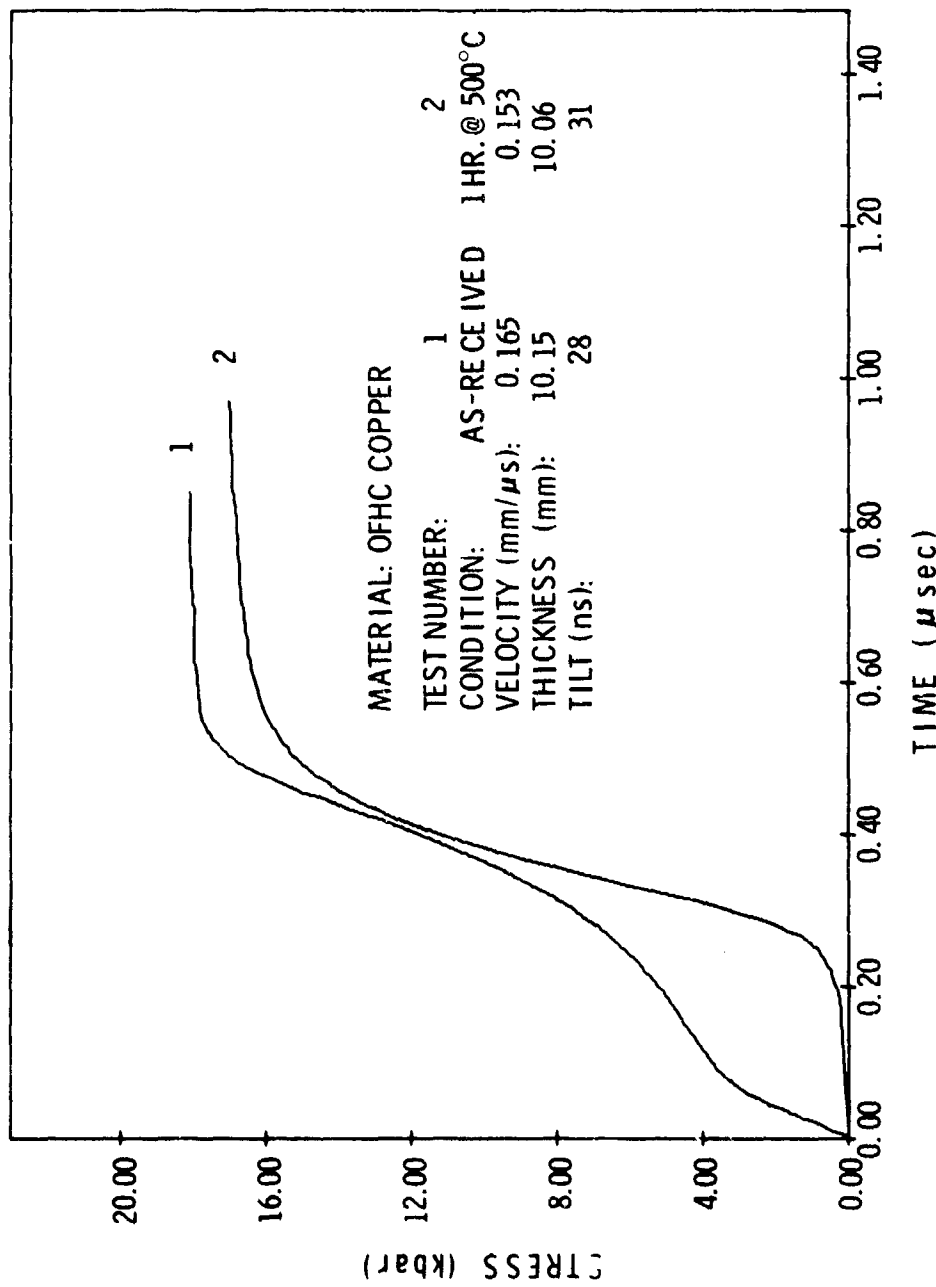


Figure 17 Compressive Waves, 1/2 Hard and Annealed Material

waves of 1 to 2 kbars amplitude (depending on crystal orientation), with fast rise time (~ 10 nsec) and stress relaxation after the elastic wave. However, for prestrained (3-1/2%) single crystals as well as polycrystalline copper they reported essentially zero yield at the wave front, with the "elastic wave" being a ramped transition to the plastic wave. This behavior was attributed to differences in dislocation densities, being estimated at $10^6/\text{cm}^2$ for the annealed material and $10^9/\text{cm}^2$ for the prestrained material.

Although the other PREDIX metals (6061-T6 aluminum, alpha titanium and tantalum) showed elastic wave risetimes less than 10 nsec, a ramped elastic wave has been observed in polycrystalline beryllium and uranium.^(48,49) Although polycrystalline beryllium has a dispersive elastic wave, single-crystal beryllium shows a fast-rising elastic wave with about a factor of 10 variation in precursor level depending on crystal orientation (with propagation along the C-axis giving the highest value). This anisotropy could contribute to smearing of the wave front in a polycrystalline material with randomly oriented grains.

Dislocation models for predicting compressive wave development utilize measurements of elastic precursor decay to evaluate various constants related to dislocation density and multiplication.⁽⁵⁰⁻⁵³⁾ Unfortunately, it is very difficult to obtain accurate elastic precursor level data at propagation distances less than ~ 2 mm and it is in this region (0 to 2 mm) that most of the precursor decay occurs for many metals of interest. Also, even at larger distances there is always some uncertainty in the precursor level due to both material scatter and dispersion characteristics and to experimental errors (particularly tilt). The result is that much of the data presently available, when given realistic uncertainty bars,

MSL-70-23, Vol. V

can be used in support of a number of different models of precursor attenuation. Copper is no exception to this, as shown in Figure 18. The calculated initial elastic impact stress was 21 kbar for these tests and the precursor level has dropped 80% to 4 kbar after only 2 mm of travel.

The data for $X > 2$ mm were obtained from quartz gage records such as those in Figure 15. Although profiles were obtained for propagation distances beyond 13 mm, it was not possible to determine a precursor level at these distances because of the excessive dispersion of the wave front. An area-monitoring gage such as quartz is obviously more sensitive to tilt than a point-monitoring gage such as the velocity interferometer which shows the deviation from elastic behavior more clearly (although the point-monitoring gage is more susceptible to anisotropic effects since the spot-size for the interferometer may be on the order of the grain size in the material). The interferometer-measured elastic waves did, however, show rise-times > 25 nsec for propagation distances > 2 mm. One velocity interferometer test with a 0.52 mm specimen gave a precursor level of 6 ± 1 kbar, which indicates that the decay curve does start to break upward sharply at 1-2 mm.

The uncertainty bars in Figure 18 reflect the dispersion and rounding at the elastic front. This spreading is due to at least two factors. First, since the quartz gage averages stress over the electrode area, small differences in wave front arrival times at the specimen/gage interface would give a finite rise-time rather than an instantaneous stress jump. These small differences in arrival times may be due to wave reflections and dispersion at grain boundaries and to slight differences in local wave velocity arising from grain anisotropy. Second, the influence of shock wave tilt on a finite-area gage is to smooth out

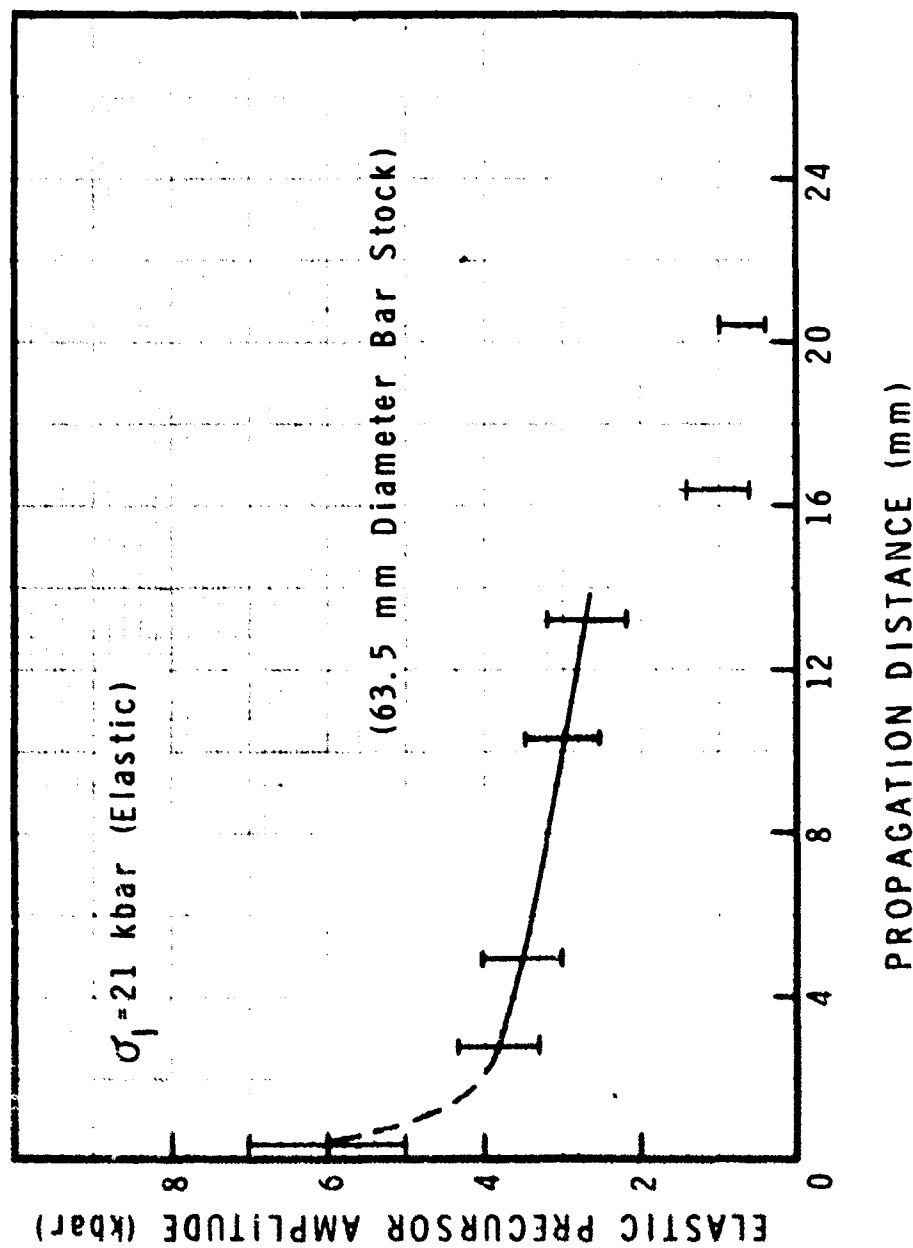


Figure 18 Elastic Precursor Decay in Copper

abrupt changes in stress level as well as to increase recording rise-time in the wave front. This becomes particularly severe at short propagation distances where separation of the elastic and plastic waves is only on the order of tens of nanoseconds. The effect of tilt is demonstrated in Figure 19. For a very low amount of tilt (4 nsec as measured across the quartz gage electrode) there is a distinct transition from the elastic to the plastic wave, while for tilt of 31 nsec the structure at the front of the wave is almost completely lost. The data have been plotted to give the same breakaway point (corresponding to wave arrival at the edge of the electrode area), which accounts for the offset between the waves in the plastic region.

RELEASE WAVES AND WAVE ATTENUATION

Release waves in copper were studied by using relatively thin copper impactors and measuring the complete wave profile with the laser velocity interferometer. After impact, elastic and plastic waves propagate from the impact surface into both impactor and target. The waves that reach the impactor free rear surface reflect as rarefaction waves, unloading the material. These unloading waves propagate across the impact surface into the target and are recorded at the target rear surface after arrival of the compressive wave. Test conditions for all velocity interferometer data discussed in this report are listed in Table III. The test numbers correspond to those listed next to each wave profile given in subsequent figures.

Unattenuated wave profiles for copper are shown in Figure 20. A fused quartz window was used on the rear of the copper target to reduce the magnitude of the unloading due to reflection of the compressive wave. This suppresses spall fracture in the

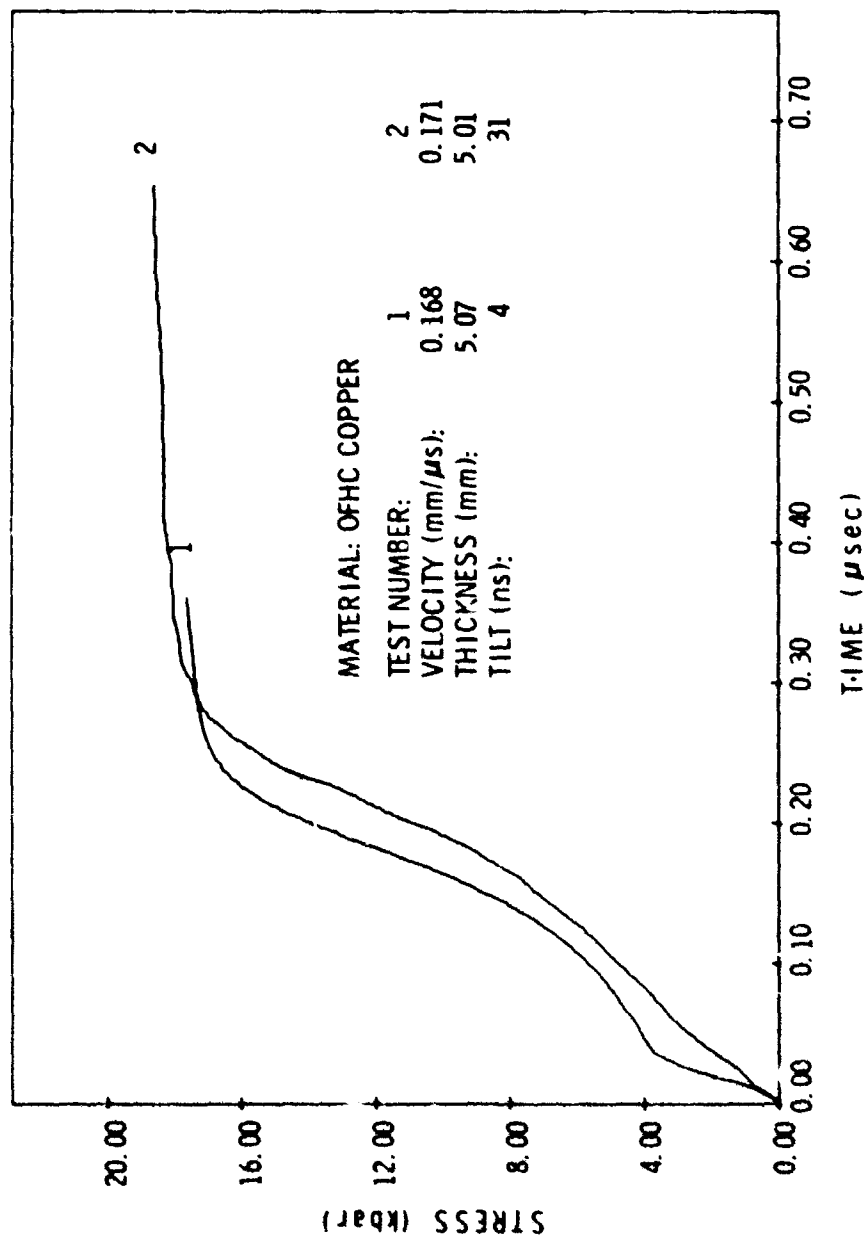


Figure 19 Effect of Tilt on Quartz Gage Records

MSL-70-23, Vol. V

TABLE III

VELOCITY INTERFEROMETER TEST DATA (20°C)

TEST NO.	V_I IMPACT VELOCITY (mm/ μ s)	X_0 IMPACTOR THICKNESS (mm)	X TARGET THICKNESS (mm)	X/X_0	CONFIG.
149	0.134	0.930	2.484	2.67	Cu-Cu
150	0.1136	1.008	2.502	2.48	Cu-Cu
151	0.217	0.881	2.499	2.84	Cu-Cu
157	0.318	0.856	2.413	2.82	Cu-Cu/FQ
158	0.217	0.983	2.512	2.56	Cu-Cu/FQ
160	0.228	0.993	5.075	5.11	Cu-Cu/FQ
161	0.227	0.919	10.117	11.01	Cu-Cu/FQ
174	0.244	0.495	3.785	7.65	Cu-Cu

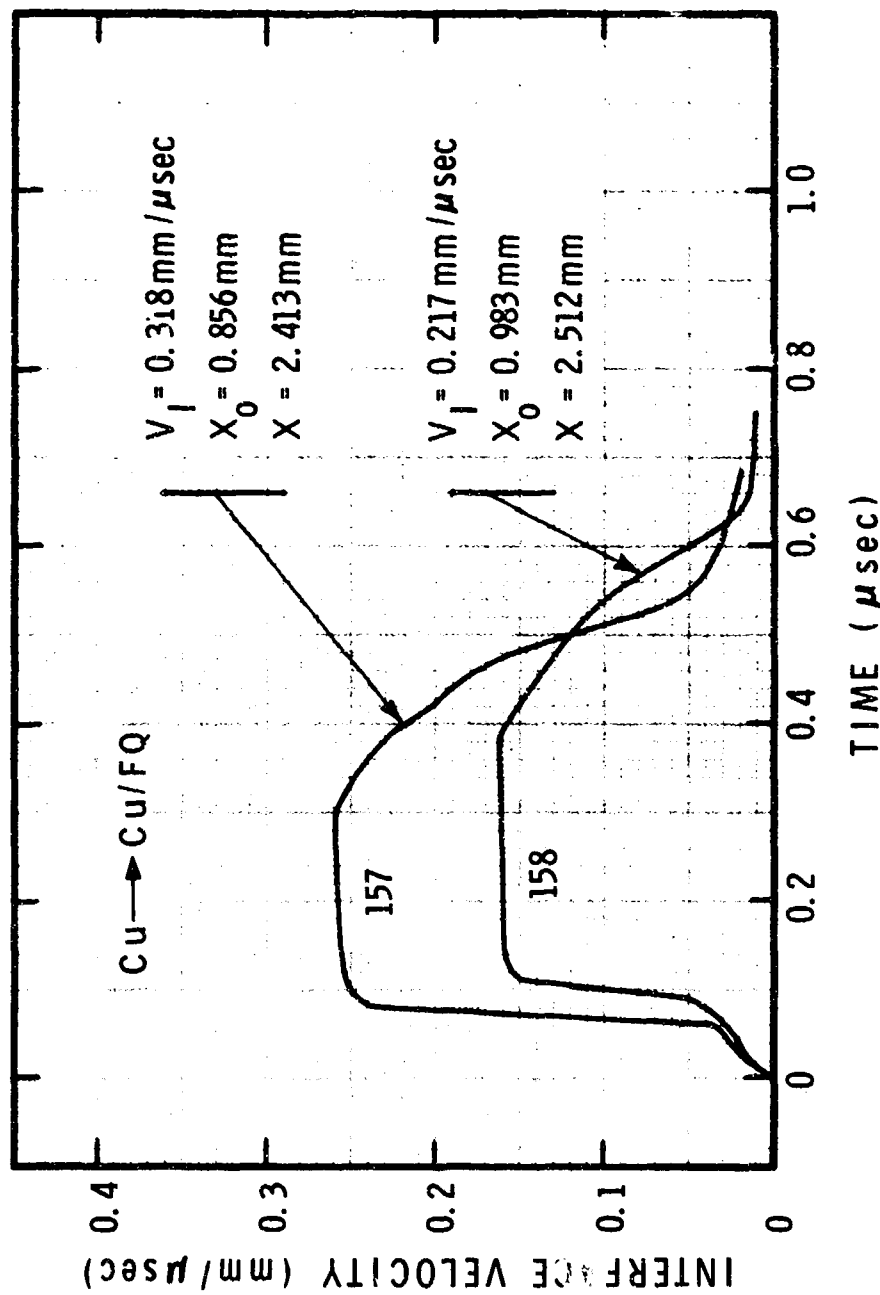


Figure 20 Wave Profiles, Stress Dependence

MSL-70-23, Vol. V

target which would prevent observation of the compressive release wave from the impactor. The measured velocity then is interface velocity, which is greater than particle velocity but less than impact velocity since the impedance of copper is greater than fused quartz. Note the ramped elastic wave, the rounded top of the plastic wave, and the structure in the release wave. This release wave structure is due to two effects. First, elastic and plastic waves have spread in the impactor before reaching the free rear surface of the impactor such that all the unloading does not occur at the same time, i.e., the unloading or release wave does not start out as an abrupt pressure drop. Secondly, additional structure may be developed due to elastic-plastic release in the material. It is difficult to separate these two contributions to release wave structure, however, the measured profiles do serve as check data for shock wave calculations.

If target thickness is great enough compared to impactor thickness, the release wave will overtake the compressive wave and attenuate the peak pressure. Wave attenuation is shown for copper in Figure 21 for an initial stress of 41 kbar. The overtaking point is between $X/X_0 = 5$ and 10, with the attenuation being $\sim 12\%$ at $X/X_0 = 11$. This is a relatively low attenuation rate compared with 6061-T6 aluminum, alpha titanium and tantalum, which show 35%, 35% and 50% attenuation respectively, at $X/X_0 = 11$ (for comparable stresses and thicknesses). (54-56)

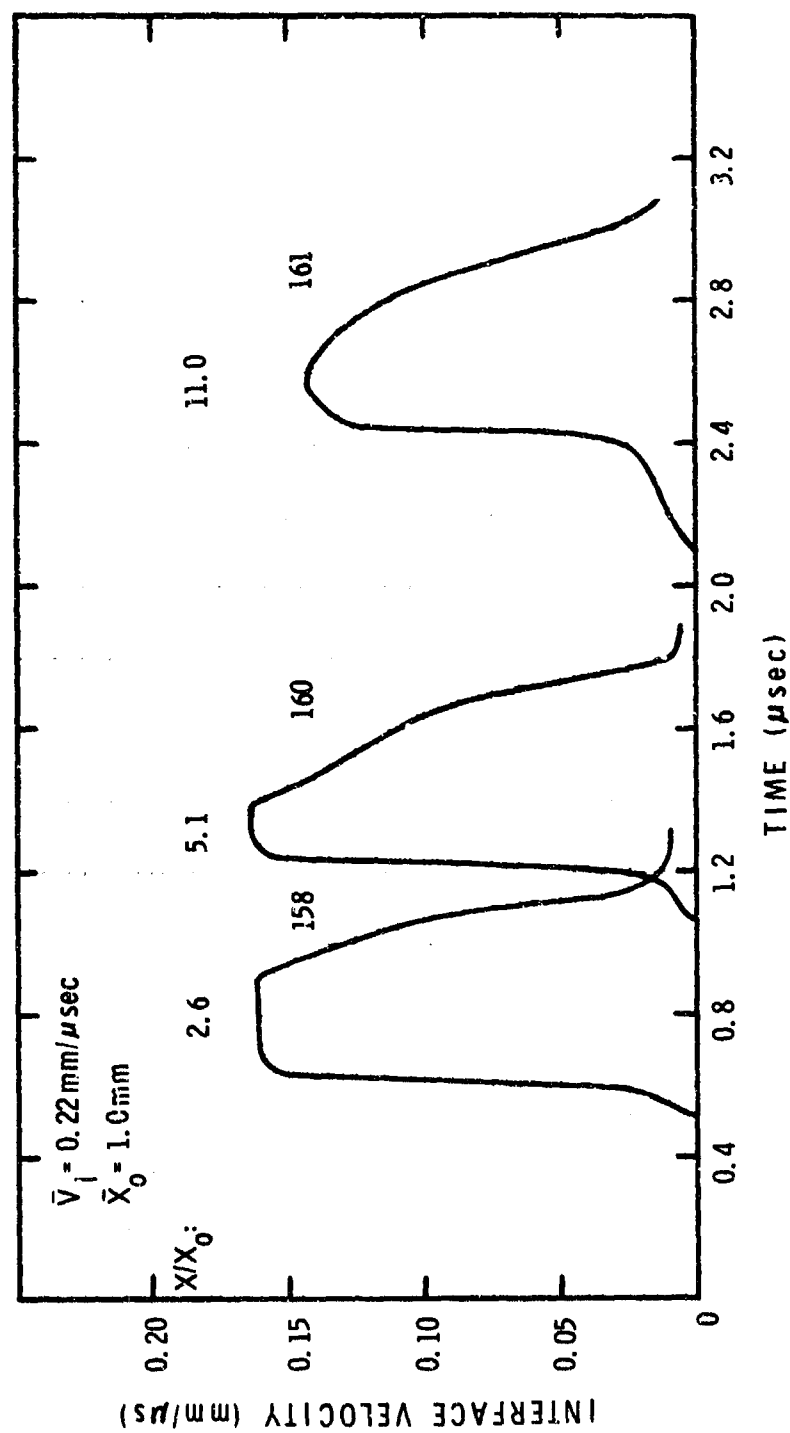


Figure 21 Wave Attenuation in Copper

SECTION VI

SPALL FRACTURE

Spall fracture by plate impact results from reflection of compressive waves from a relatively low impedance interface (normally a free surface) and their subsequent interaction. Spall studies were carried out with both passive and active techniques. Passive methods involve the recovery and examination of shock-loaded specimens. Metallographic examination establishes the type and degree of damage, which can be correlated with impact parameters such as velocity, impactor thickness and target thickness. Active methods utilize the laser velocity interferometer and provide quantitative, time-resolved data on the influence of internal fractures or spall surfaces on shock wave profiles, as measured at the rear surface.

RECOVERY TESTS

The spall behavior of copper was studied by carrying out a series of impact and recovery tests, where the target was sectioned across a diameter, polished, etched and examined optically at a magnification of $\sim 50X$. The specimens were then graded or classified according to the degree of fracture that was observed, which ranged from no visible damage to complete material separation. The incipient spall threshold was defined as the impact velocity (for a given set of impact parameters) corresponding to cracking over at least 50% of the width of the section estimated to be under a condition of plane

strain during the time of loading. The specimens were polished and etched to provide maximum contrast between cracks and sound material. The procedure followed was:

1. Wet grind, 320/400/600 grit silicon carbide paper.
2. Rough polish, 6 μm diamond paste on rayon cloth.
3. Final polish, 1 μm diamond paste on rayon cloth.
4. Etch, equal parts water (H_2O), hydrogen peroxide (3% H_2O_2) and ammonium hydroxide (NH_4OH), 10-20 sec swab etch, 20°C.

Optical photomicrographs of recovered specimens are shown in Figures 22 and 23. Fracture is of a ductile nature with the development of individual voids. As impact velocity increases, the number of voids becomes greater but their size increases only slightly. At high enough velocities, the voids begin to coalesce and a complete fracture surface is formed. Note that as velocity increases, the voids tend to cluster within a very narrow band with only a few small voids outside this band. Although no correlation has been proven, copper has a poorly-defined, low-amplitude elastic wave and shows a definite "spall plane", while the other PREDIX metals⁽⁵⁴⁻⁵⁶⁾ which have well-defined elastic wave structures show considerable dispersion of the spall plane, as demonstrated in Figure 24. This behavior can probably be related to differences in tensile stress history in the region of the "nominal" spall plane. For copper, the average distance from the spall plane to the target rear surface* was approximately equal to the impactor thickness, for unattenuated pulses. A comparison of spall fracture in sectioned specimens as observed by optical and scanning electron microscopy is

* All spall photomicrographs in this report have the target rear surface at the top of the picture.

MSL-70-23, Vol. V

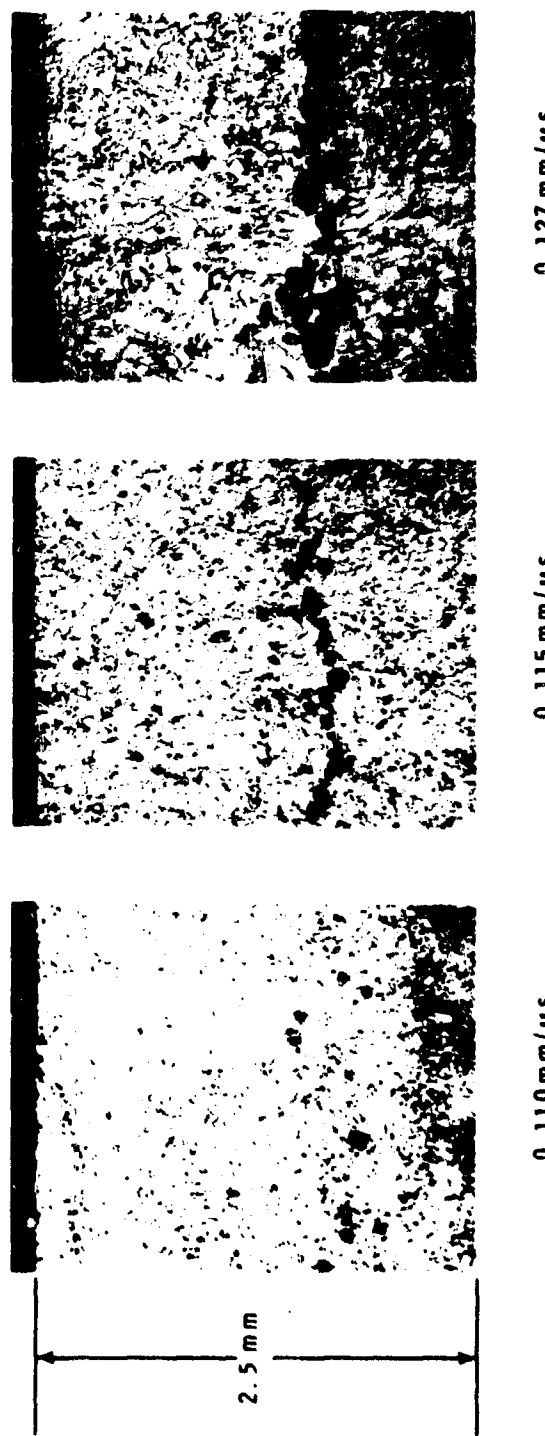


Figure 22 Spall Fractures in Copper
(1.5 mm + 3.0 mm)

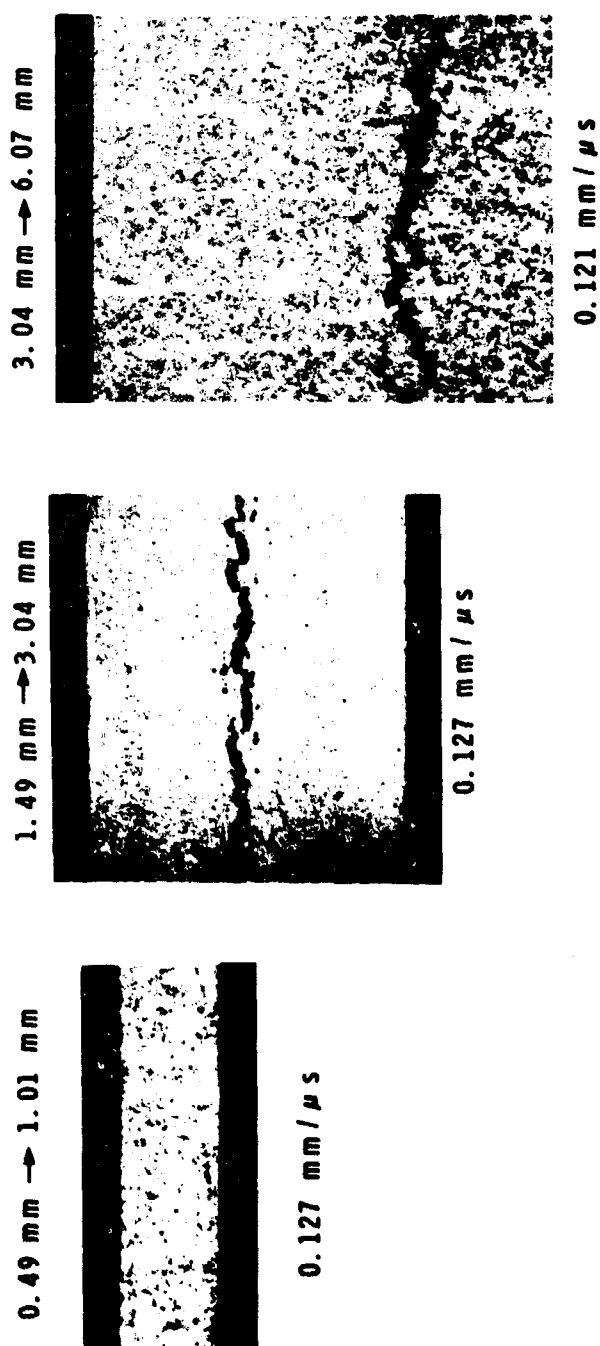


Figure 23 Spall Fractures in Copper

MANUFACTURING DEVELOPMENT • GENERAL MOTORS CORPORATION

MSL-70-23, Vol. V

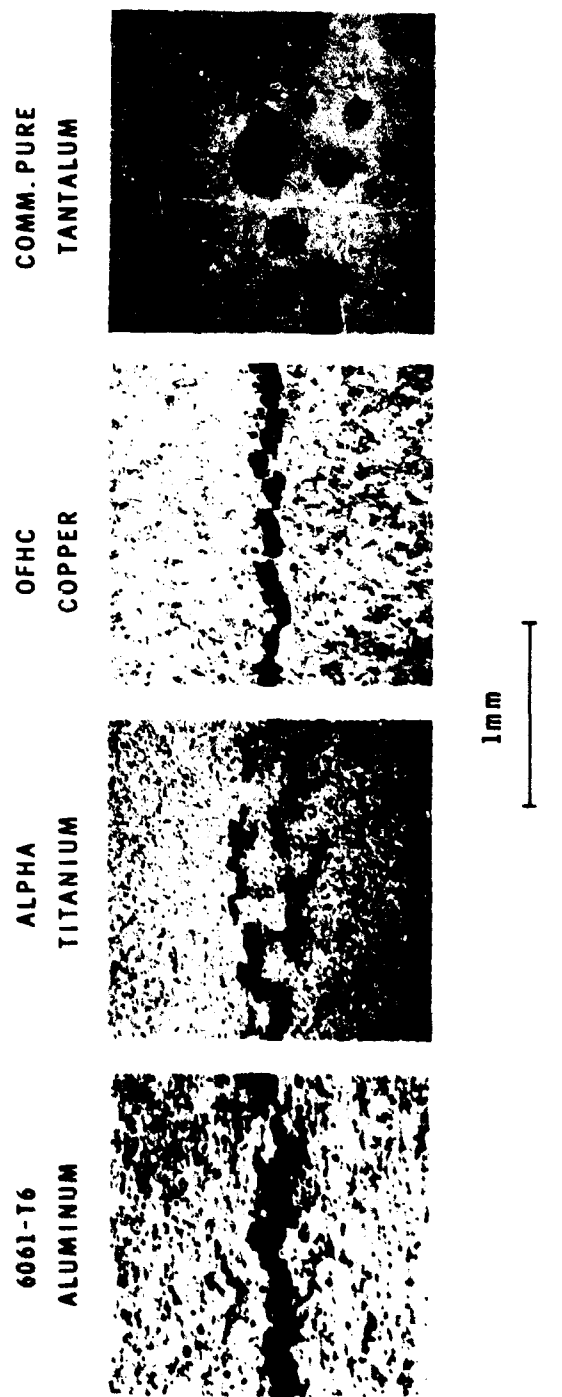


Figure 24 Spall Fractures in Metals

given in Figure 25. Although the greater depth of field of the SEM gives more detail in and around the voids (particularly at higher magnifications) the optical microscope is adequate for general examination and determination of the spall threshold.

Scanning microfractographs of the fracture surface for a completely separated specimen are shown in Figure 26. The equiaxed nature of the dimples indicates failure by a normal rupture process, where the voids have grown and coalesced under the action of plastic strain in the direction of wave propagation. The dimples are relatively deep and the walls show a rippled structure due to deformation or stretching. These ripples may be serpentine glide patterns resulting from intersection of slip planes with the void walls during growth.

Spall data for all tests with unattenuated pulses ($X/X_0 \approx 2$) are given in Figure 27. The symbols are defined as:

- Complete Separation
- ◐ Above Incipient
- Incipient Spall
- ◑ Below Incipient
- No Visible Damage

As is typically the case with metals, the impact velocity for incipient spall increases for decreasing impactor thickness. This implies that the peak stress (and, therefore, strain) required to create spall fracture increases with decreasing pulse width or time of loading. The incipient spall results from all tests, including an attenuated wave series, are summarized in Table IV.

MSL-70-23, Vol. V

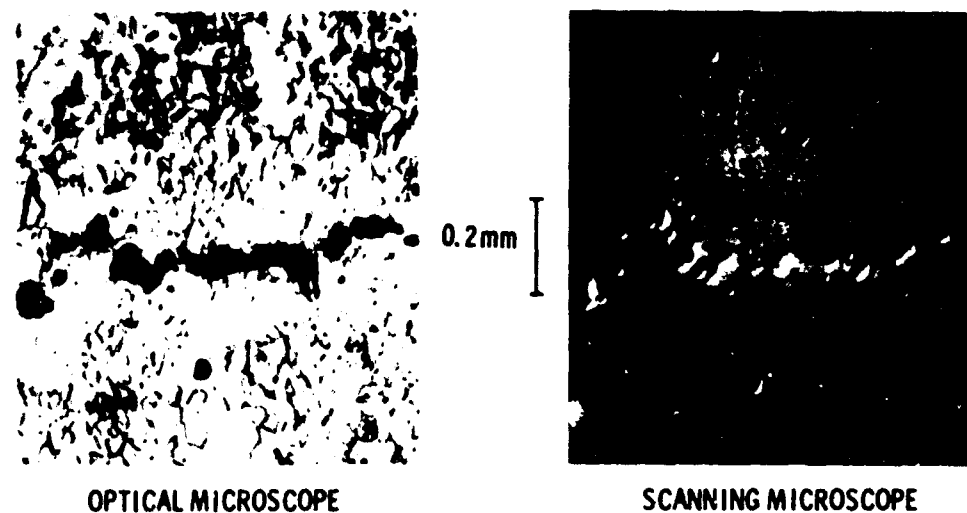


Figure 25 Spall Fractures in Copper
(1.5 mm + 3.0 mm, 0.115 mm/μs)

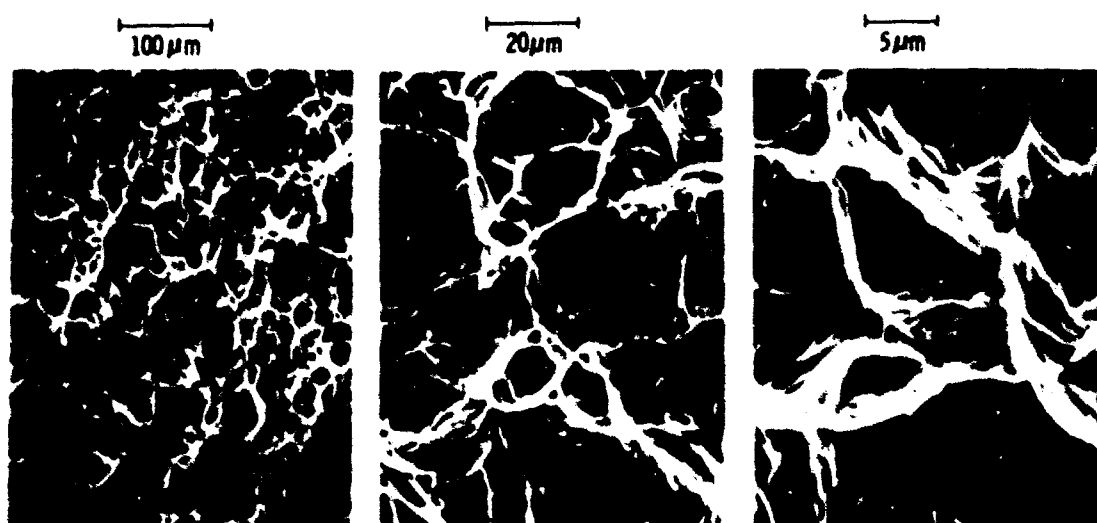


Figure 26 Spall Fracture Surface in Copper
(0.5 mm + 1.0 mm, 0.181 mm/μs)

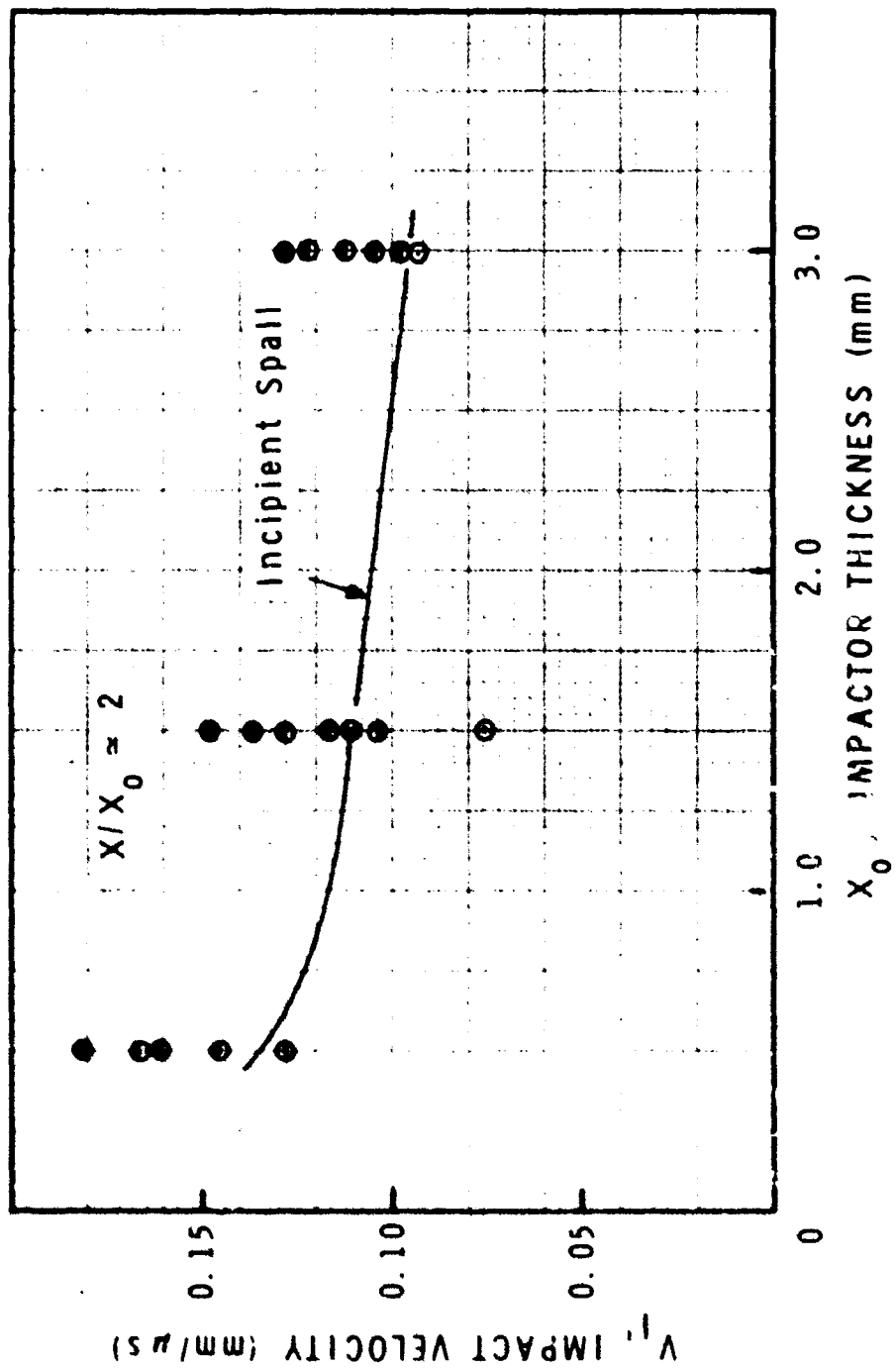


Figure 27 Spall Data for Copper

MSL-70-23, Vol. V

TABLE IV

INCIPIENT SPALL DATA FOR COPPER (20°C)

x_0 IMPACTOR THICKNESS (mm)	X TARGET THICKNESS (mm)	x/x_0	Δt_e PULSE WIDTH* (μ s)	v_s SPALL VELOCITY (mm/ μ s)
0.49	1.01	2.06	0.21	0.135
1.49	3.04	2.04	0.63	0.110
3.04	6.07	2.00	1.28	0.095
0.40	3.85	9.63	0.17	0.180

$$* \Delta t_e = \frac{2x_0}{C_L}$$

Spall data for copper reported by Smith⁽⁵⁷⁾ showed similar time dependence as the present work but a lower incipient spall level. This is probably due to a softer material ($R_F = 68$ for Smith's copper) and an incipient spall criteria based on initial void appearance.

SPALL PROFILES

Spall wave profiles were studied using a copper-into-copper configuration, as in the wave profile tests, but with a free rear surface on the target for complete reflection of the compressive front. Measured profiles for unattenuated pulses are shown in Figure 28, with photomicrographs of the recovered and sectioned targets. Also shown for reference are the incipient and complete spall levels for this impactor/target combination as determined from the recovery tests. Evidence of fracture in the target is shown as a reversal of the measured release wave. This occurs as the rarefaction wave is reflected from the spall plane as a compressive wave which then reaches the rear surface and gives it a positive velocity increment. As this "trapped" wave reverberates back and forth between the spall plane and the rear surface, a sinusoidal-type motion is observed. This motion eventually damps out due to dispersion and attenuation in the material and to the effects of edge rarefactions.

The amount of pullback (decrease in free surface velocity to the point of first reversal) may be related to the tensile strength at the spall plane of the material for a given impact geometry. An empirical relation for this is given by: ⁽⁴⁹⁾

$$\sigma_s = \rho C (\Delta u_{fs} / 2) \quad (26)$$

where σ_s is tensile strength, ρ and C are local density and longitudinal wave speed, and Δu_{fs} is pullback.

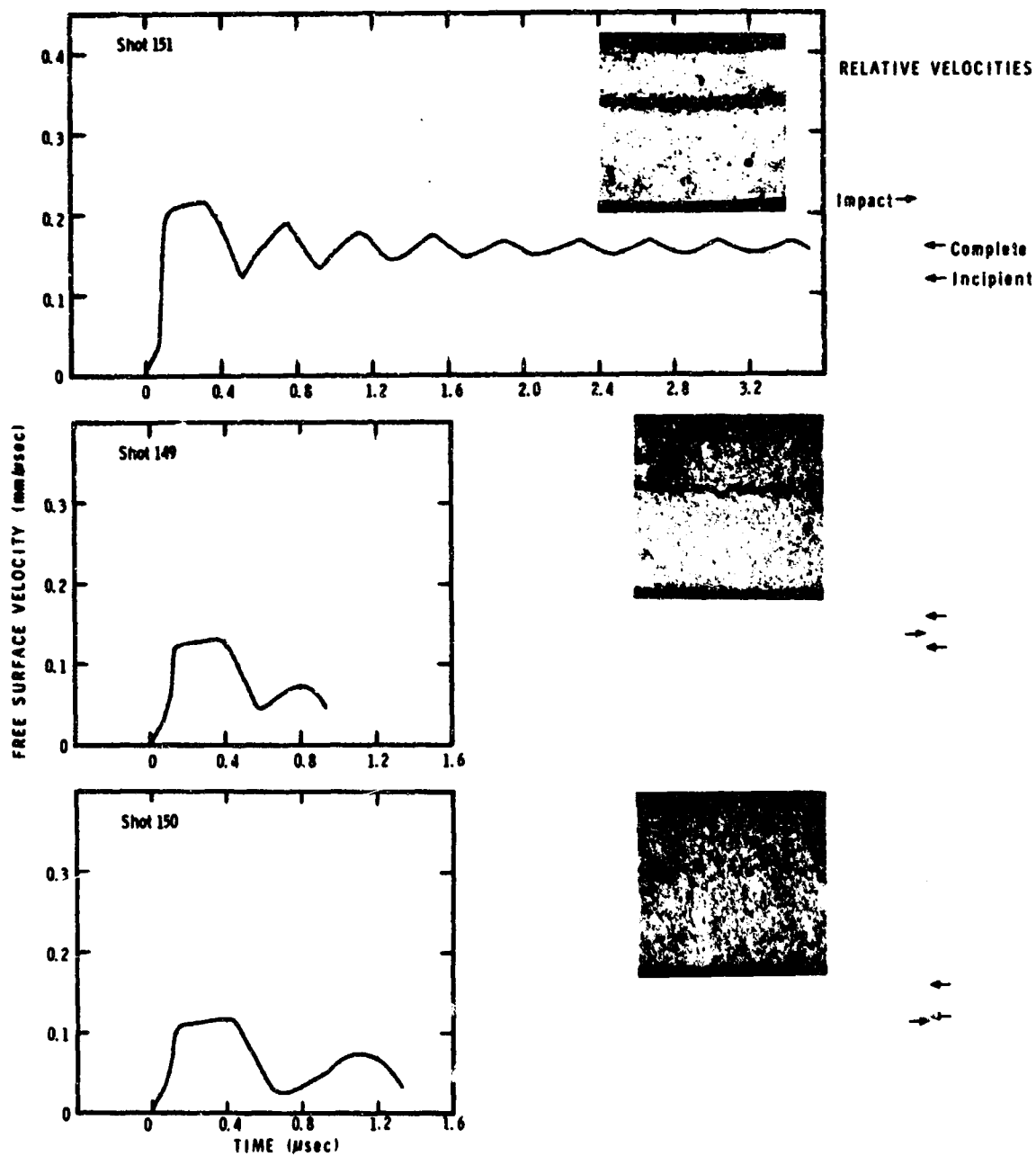


Figure 28 Spall Wave Profiles in Copper
(1 mm + 2.5 mm)

The data in Figure 28 give $\sigma_s \approx 21$ kbar. Note that the pull-back is relatively insensitive to peak compressive stress. This calculated spall strength is not constant for a given material since it is proportional to Δu_{fs} which has been found to change with such factors as pulse width, pulse shape and target temperature. (58)

The spall profile for an attenuated pulse, where the time duration of the peak tensile stress is expected to be less than for the unattenuated case, is shown in Figure 29. The pullback for this case is 0.16 μ sec giving a spall strength of ~ 35 kbar, consistent with time-dependency of spall fracture shown in Figure 27.

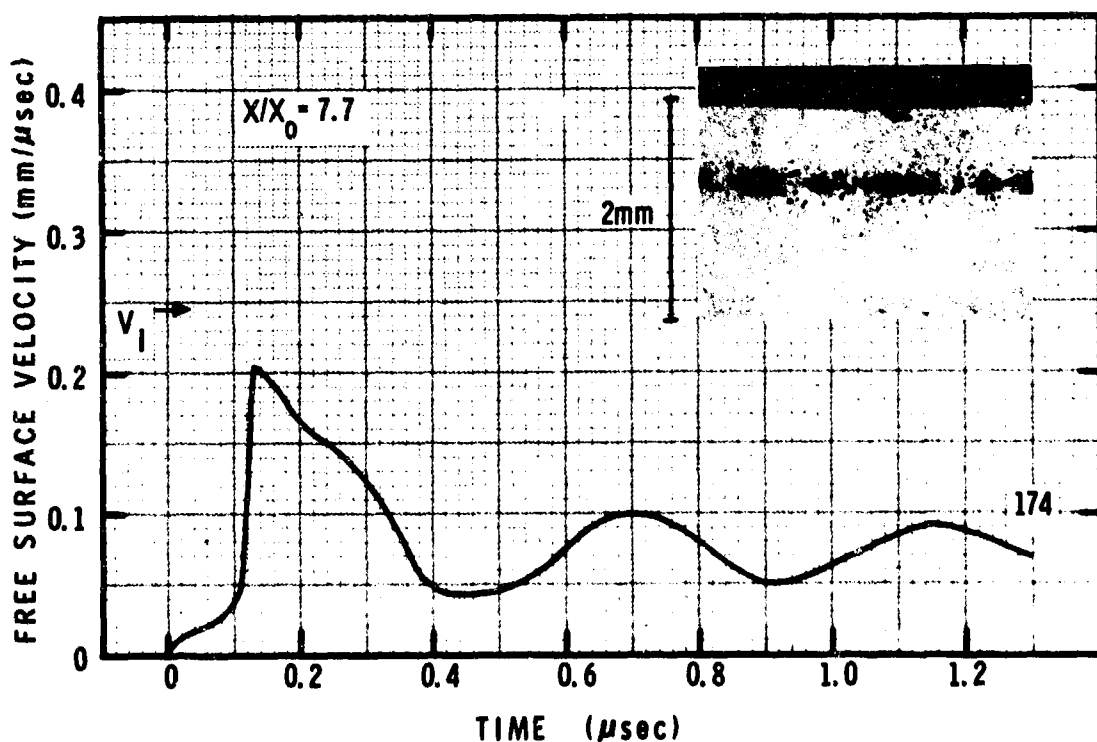


Figure 29 Attenuated Spall Wave Profile in Copper

MSL-70-23, Vol. V

SUMMARY

The dynamic properties of OFHC copper have been measured under uniaxial stress and uniaxial strain conditions. The material tested was 1/2-hard bar stock with $\sim 64 \mu\text{m}$ grain size and $78R_F$ hardness. Material response to compressive uniaxial stress deformation approximated elastic-perfectly plastic behavior. There was slight rate sensitivity with ~ 2.7 kbar yield at 0.005/sec and ~ 3.2 kbar yield at 950/sec. Annealing reduced the yield to ~ 0.25 kbar but increased the work-hardening exponent by almost an order of magnitude.

Longitudinal and shear wave velocities were measured as functions of temperature and pressure, giving the following (in $\text{mm}/\mu\text{sec}$):

$$C_L = 4.766 - (0.000434 \times T)$$

$$C_S = 2.253 - (0.000300 \times T)$$

(T in $^{\circ}\text{C}$)

$$C_L = 4.757 + (0.01585 \times P)$$

$$C_S = 2.247 + (0.00243 \times P)$$

(P in kbar)

Principal elastic constants were evaluated at $T = 20^{\circ}\text{C}$ and $P = 0$, including:

Bulk Modulus = K_0^S = 1418 kbar

$$\left(\frac{\partial K^S}{\partial P}\right)_S = 5.40, \quad \left(\frac{\partial K^S}{\partial P}\right)_T = 5.53$$

Shear Modulus = G_0^S = 450 kbar

$$\left(\frac{\partial G^S}{\partial P}\right)_S = 1.24, \quad \left(\frac{\partial G^S}{\partial P}\right)_T = 1.30$$

Poisson's Ratio = 0.356

Elastic wave velocity data were also used in determining the Gruneisen parameter γ and the Debye temperature θ :

$$\gamma = 2.13 @ T = 20^\circ\text{C} \text{ and } P = 0$$

$$\frac{\partial \gamma}{\partial T} = -0.00076/\text{°C} @ T = 20^\circ\text{C}$$

$$\frac{\partial \gamma}{\partial P} = -0.0020/\text{kbar} @ P = 0$$

$$\theta = 331^\circ\text{K}$$

The shock wave hugoniot was determined experimentally to be:

$$\sigma_H = 1.5 + 344 u_p + 143 u_p^2 \quad (\sigma_H < 200 \text{ kbar})$$

Assumption of an ideal elastic-plastic wave structure with an 8 kbar hugoniot elastic limit and equilibrium initial and final states gave:

$$\sigma_H = 3.1 + 1308\mu + 3520\mu^2$$

MSL-70-23, Vol. V

$$P_H = 1308 \mu + 3520 \mu^2$$

$$U_S = 3.915 + 1.53 u_p$$

The hydrostat as determined from elastic constants data was:

$$P_H = 1025 \left[\left(\frac{1+\mu}{1-\mu} \right)^{2.73} - 1 \right] - 1383 \ln \left(\frac{1+\mu}{1-\mu} \right) + 1611 \left(\frac{\mu}{1+\mu} \right)^3$$

(Keane equation of state)

Measurements of compressive wave development showed the wave front to be characterized by a non-steady-state elastic portion and a transition to a spreading plastic wave. Elastic precursor attenuation was rapid, decaying 80% to 4 kbar after only 2 mm of travel. Dispersion of the elastic wave was so great that meaningful values for the precursor level could not be obtained for propagation distances greater than ~ 13 mm. Copper showed a relatively low shock wave attenuation rate, with a 41 kbar, 0.5 μ sec pulse attenuating only 12% at $X/X_0 = 11$.

The spall behavior was determined for elastic pulse widths of 0.21, 0.63 and 1.28 μ sec. The incipient spall threshold expressed as impact velocity increased with decreasing pulse width. Copper showed a very well-defined spall plane with void formation and growth confined to a relatively narrow band. For unattenuated pulses, the spall plane was located approximately one impactor thickness from the target rear surface. The fracture surface for completely spalled copper showed ductile failure characterized by equiaxed dimples with evidence of serpentine glide at the void walls.

ACKNOWLEDGMENTS

The authors wish to thank Dr. T. E. Michaels and Mr. A. R. McMillan for contributions to the equation of state and wave propagation studies, Mr. F. L. Schierloh for assistance in the strain rate work, and Dr. B. Taylor for the transmission electron microscopy. Also, the assistance of the following Materials and Structures Laboratory personnel in the experimental work is gratefully recognized: Mr. B. Bielski and Mr. J. Wigton for specimen preparation; Mr. F. Feistmann, Mr. F. Stemczynski and Mr. E. Miller for EOS and wave profile tests; Mr. J. Havens for ultrasonics measurements; Mr. C. Woodcock for spall tests; Mr. J. Borner and Mr. H. Simmons for strain rate tests; Mr. C. Whitchurch and Mr. L. Seltz for metallographic work; and Mrs. W. Trippen and Mrs. C. Strong for data analysis.

REFERENCES

1. "A Selected Bibliography on Dynamic Properties of Materials", compiled by Christman, D. R., General Motors Corporation, Manufacturing Development, Materials and Structures Laboratory, DASA 2511, June, 1970 (AD 710823).
2. Metals Handbook, 8th. Ed., Vol. 1: Properties and Selection of Metals, Lyman, T., Ed., American Society for Metals, Metals Park, Ohio, 1961.
3. Handbook of Chemistry and Physics, 45th. Ed., Weast, R. C., Ed., The Chemical Rubber Co., Cleveland, Ohio, 1964.
4. Thermophysical Properties of High Temperature Solid Materials, Vol. 1: Elements, Touhoukian, Y. S., Ed., The McMillan Co., New York, N.Y., 1967.
5. Babcock, S. G., Langan, J. J., Norvey, D. B., Michaels, T. E. and Schierloh, F. L., "Characterization of Three Aluminum Alloys", General Motors Corporation, Manufacturing Development, Materials and Structures Laboratory, MSL-70-12, May, 1970.
6. Maiden, C. J. and Green, S. J., "Compressive Strain-Rate Tests on Six Selected Materials at Strain Rates from 10^{-3} to 10^4 In/In/Sec", ASME Trans.-J. Appl. Mech., Ser. E, Vol. 33, p. 496-504, 1966.
7. Kumar, A. and Kumble, R. G., "Viscous Drag on Dislocations at High Strain Rates in Copper", J. Appl. Phys., Vol. 40, p. 3475-3480, 1969.
8. Green, S. J., Maiden, C. J., Babcock, S. G. and Schierloh, F. L., "The High Strain-Rate Behavior of Face Centered Cubic Materials", General Motors Corporation, Manufacturing Development, Materials and Structures Laboratory, MSL-69-36, Oct., 1969.
9. Wonsiewicz, B. C. and Chin, G. Y., "Plain Strain Compression of Copper, Cu6WtPctAl, and Ag4WtPctSn Crystals", Met. Trans., Vol. 1, p. 2715-2722, 1970.
10. Morrow, J., "Cyclic Plastic Strain Energy and Fatigue of Metals", Internal Friction, Damping and Cyclic Plasticity, STP 378, American Society for Testing and Materials, p. 45-87, 1965.

11. Hecker, S., Private Communication, General Motors Research Laboratories, 1970.
12. Salama, K. and Alers, G. A., "Third Order Elastic Constants of Copper at Low Temperature", Phys. Rev., Vol. 161, p. 643-680, 1967.
13. Chang, Y. A. and Himmel, L, "Temperature Dependence of the Elastic Constants of Cu, Ag, and Au Above Room Temperature", J. Appl. Phys., Vol. 37, p. 3567-3572, 1966.
14. Kolsky, H., Stress Waves in Solids, S1098, Dover Publications, Inc., New York, N. Y. 1963.
15. Mason, W. P., "Acoustic Properties of Solids", American Institute of Physics Handbook, 2nd. Ed., p. 3-28 - 3-97, 1963.
16. Barsch, G. R. and Chang, Z. P., "Adiabatic, Isothermal, and Intermediate Pressure Derivatives of the Elastic Constants for Cubic Symmetry", Phy. Stat. Sol., Vol. 19, p. 129-151, 1967.
17. Walsh, J. M., Rice, M. H., McQueen, R. G. and Yarger, F. L., "Shock-Wave Compressions of Twenty-Seven Metals, Equation of State of Metals", Phys. Rev., Vol. 108, p. 196-216, 1957.
18. Slater, J. C., Introduction to Chemical Physics, McGraw-Hill Book Co., New York, N. Y., 1939.
19. Dugdale, J. S. and MacDonald, D. K. C., "The Thermal Expansion of Solids", Phys. Rev., Vol. 89, p. 832-834, 1953.
20. Schreiber, E. and Anderson, O. L., "Pressure Derivatives of the Sound Velocities of Polycrystalline Alumina", Am. Ceram. Soc. J., Vol. 49, p. 184-190, 1966.
21. Anderson, O. L. and Dienes, G. J., Non-Crystalline Solids (Chapter 18), Ed. by Frechette, V. D., John Wiley and Sons, New York, 1960.
22. Schuele, D. E. and Smith, C. S., "Low Temperature Thermal Expansion of RbI", J. Phys. Chem. Solids, Vol. 25, p. 801-814, 1964.
23. McQueen, R. G. and Marsh, S. P., "Equation of State for Nineteen Metallic Elements from Shock-Wave Measurements to Two Megabars", J. Appl. Phys., Vol. 31, p. 1253-1269, 1960.

MSL-70-23, Vol. V

24. Anderson, O. L., "A Simplified Method for Calculating the Debye Temperature from Elastic Constants", J. Phys. Chem. Solids, Vol. 24, p. 909-917, 1963.
25. Alers, G. A., "Use of Sound Velocity Measurements in Determining the Debye Temperature of Solids", Physical Acoustics, Vol. III, Part B (Lattice Dynamics), Academic Press, New York, N.Y., p. 1-42, 1965.
26. Munson, D. E. and Barker, L. M., "Dynamically Determined Pressure-Volume, Relationships for Aluminum, Copper and Lead", J. Appl. Phys., Vol. 37, p. 1652-1660, 1966.
27. Isbell, W. M., Shipman, F. H. and Jones, A. H., "Hugoniot Equation of State Measurements for Eleven Materials to Five Megabars", General Motors Corporation, Manufacturing Development, Materials and Structures Laboratory, MSL-68-13, December, 1968; also see MSL-71-12, April, 1971.
28. Overton, W. C., "Relation Between Ultrasonically Measured Properties and the Coefficients in the Solid Equation of State", J. Chem. Phys., Vol. 37, p. 116-119, 1962.
29. Anderson, O. L., "The Use of Ultrasonic Measurements Under Modest Pressures to Estimate Compression at High Pressures", J. Phys. Chem. Solids, Vol. 27, p. 547-565, 1966.
30. Lamberson, D. L., "The High Pressure Equation of State of Tantalum, Polystyrene and Carbon Phenolic Determined from Ultrasonic Velocities", Doctoral Dissertation, Air Force Institute of Technology (AFIT-SE), Wright-Patterson AFB, Ohio, March, 1969.
31. MacDonald, J. R., "Review of Some Experimental and Analytical Equations of State", Rev. Mod. Phys., Vol. 41, p. 316-349, 1969.
32. Birch, F., "The Effect of Pressure Upon the Elastic Parameters of Isotropic Solids, According to Murnaghan's Theory of Finite Strain", J. Appl. Phys., Vol. 9, p. 279-288, 1938.
33. Birch, F., "Elasticity and Constitution of the Earth's Interior", J. Geophys. Res., Vol. 57, p. 227-286, 1952.
34. Murnaghan, F. D., "The Compressibility of Media Under Extreme Pressures", Proc. Nat. Ac. Sci., Vol. 30, p. 244-247, 1944.

35. Keane, A., Australian J. Phys., Vol. 1, p. 323, 1954.
36. Anderson, O. L., "On the Use of Ultrasonic and Shock-Wave Data to Estimate Compressions at Extremely High Pressures", Phys. Earth Planet. Interiors, Vol. 1, p. 169-176, 1968.
37. Duvall, G. E. and Zwolinski, B. J., "Entropic Equations of State and Their Applications to Shock Wave Phenomena in Solids", Acoust. Soc. Am. J., Vol. 27, p. 1051-1058, 1955.
38. Zel'dovich, Y. B. and Raizer, Y. P., Physics of Shock Waves and High-Temperature Hydrodynamic Phenomena, Vol. II, Academic Press, New York, N.Y., p. 688-709, 1967.
39. Ruoff, A. L., "Linear Shock-Velocity-Particle-Velocity Relationship", J. Appl. Phys., Vol. 38, p. 4976-4980, 1967.
40. Pastore, D. J. and Piacesi, D., "The Existence and Implications of Curvature in the Relation Between Shock and Particle Velocities for Metals", J. Phys. Chem. Solids, Vol. 27, p. 1783-1792, 1966.
41. Smith, C. S., "Metallographic Studies of Metals after Explosive Shock", AIIM Trans., Vol. 212, p. 574-589, 1958.
42. Appleton, A. S. and Waddington, J. S., "The Importance of Shock Wave Profile in Explosive Loading Experiments", Acta Met., Vol. 12, p. 956-957, 1964.
43. Higgins, G. T., "The Structure and Annealing Behavior of Shock-Loaded, Cube-Oriented Copper", Metall. Trans., Vol. 2, p. 1277-1282, 1971.
44. Johari, O. and Thomas, G., "Substructures in Explosively Deformed Cu and Cu-Al Alloys", Acta Met., Vol. 12, p. 1153-1159, 1964.
45. Brillhart, D. C., DeAngelis, R. J., Preban, A. G., Cohen, J. B. and Gordon, F., "Quantitative Study of the Substructure and Properties of Shock-Loaded Copper", AIIM Trans., Vol. 239, p. 836-843, 1967.
46. Murr, L. E. and Grace, F. I., "Defect Microstructure and Mechanical Properties in Shock-Hardened Metals", Exp. Mech., Vol. 9, p. 145-155, 1969.
47. Jones, O. E. and Mote, J. D., "Shock-Induced Dynamic Yielding in Copper Single Crystals", J. Appl. Phys., Vol. 40, p. 4920-4923, 1969.

MSL-70-23, Vol. V

48. Christman, D. R. and Froula, N. H., "Dynamic Properties of High-Purity Beryllium", AIAA J., Vol. 8, p. 477-482, 1970.
49. Taylor, J. W., "Stress Wave Profiles in Several Metals", Dislocation Dynamics, McGraw-Hill Book Co., New York, N.Y., p. 573-589, 1968.
50. Taylor, J. W., "Dislocation Dynamics and Dynamic Yielding", J. Appl. Phys., Vol. 36, p. 3146-3150, 1965.
51. Gilman, J. J., "Dislocation Dynamics and the Response of Materials to Impact", Appl. Mech. Rev., Vol. 21, p. 767-783, 1968.
52. Johnson, J. N., "Constitutive Relation for Rate-Dependent Plastic Flow in Polycrystalline Metals", J. Appl. Phys., Vol. 40, p. 2287-2293, 1969.
53. Read, H. E., Triplett, J. R. and Cecil, R. A., "Dislocation Dynamics and the Formulation of Constitutive Equations for Rate Dependent Plastic Flow in Metals", Systems, Science, and Software, DASA 2638, December, 1970.
54. Isbell, W. M., Christman, D. R., Babcock, S. G., McMillan, A. R. and Green, S. G., "Measurements of Dynamic Properties of Materials, Vol. III: 6061-T6 Aluminum", General Motors Corporation, Manufacturing Development, Materials and Structures Laboratory, DASA 2501-3, 1971.
55. Christman, D. R., Michaels, T. E., Isbell, W. M. and Babcock, S. G., "Measurements of Dynamic Properties of Materials, Vol. IV: Alpha Titanium", General Motors Corporation, Manufacturing Development, Materials and Structures Laboratory, DASA 2501-4, 1971.
56. Isbell, W. M., Christman, D. R. and Babcock, S. G., "Measurements of Dynamic Properties of Materials, Vol. VI: Tantalum", General Motors Corporation, Manufacturing Development, Materials and Structures Laboratory, DASA 2501-6, 1971.
57. Smith, J. H., "Three Low-Pressure Spall Thresholds in Copper", Dynamic Behavior of Materials, American Society for Testing Materials, Philadelphia, P. 264-282, 1963.
58. Isbell, W. M. and Christman, D. R., "Shock Propagation and Fracture in 6061-T6 Aluminum from Wave Profile Measurements", General Motors Corporation, Manufacturing Development, Materials and Structures Laboratory, DASA 2419, April, 1970 (AD705536).

APPENDIX A

ELASTIC CONSTANTS EQUATIONS

Following are the equations used in calculating various elastic constants and the adiabatic and isothermal pressure and temperature derivatives of the bulk and shear modulii (K and G):

$$C_B = \sqrt{C_L^2 - 4/3 C_S^2}$$

(Bulk Wave Velocity)

$$C_E = \sqrt{2(1+\nu) C_S^2}$$

(Sound wave velocity, longitudinal
wave of infinite wave length in
bar, lateral displacement allowed)

$$C_R: k_1^6 - 8k_1^4 + (24 - 16\nu^2)k_1^2 + (16\nu^2 - 16) = 0$$

$$\text{where } k_1^2 = (C_R/C_S)^2, \nu^2 = (C_S/C_L)^2$$

(Rayleigh or Surface Wave Velocity)

* The expressions for the pressure derivatives are simplified in these equations, e.g.,

$$K_{OS}' = \left(\frac{\partial K^S}{\partial P} \right)_S \bigg|_{P=0}$$

MSL-70-23, Vol. V

$$\nu = [0.5 - (C_S/C_L)^2]/[1.0 - (C_S/C_L)^2]$$

(Poisson's Ratio)

$$K = \rho C_B^2 = \rho (C_L^2 - 4/3 C_S^2)$$

(Bulk Modulus)

$$G = \rho C_S^2$$

(Shear or Rigidity Modulus)

$$E = 2\rho(1+\nu) C_S^2$$

(Young's or Elastic Modulus)

$$\lambda = 2\rho\nu C_S^2/(1-2\nu)$$

(Lamé's Parameter)

$$K_0^T = \frac{K_0^S}{1 + \beta \gamma_0 T}$$

$$\text{where } \gamma_0 = \frac{\beta K_0^S}{\rho_0 c_p}$$

$$K_{0S}' = K_{0T}' + \left(\frac{\partial K^S}{\partial T} \right)_0 \left(\frac{\gamma_0 T}{K_0^S} \right)$$

$$K_{0T}^{T'} = K_{0T}^{S'} + \beta \gamma_0 T \left(\frac{K_0^T}{K_0^S} \right) \left[1 - \frac{2}{\beta K_0^T} \left(\frac{\partial K^T}{\partial T} \right)_0 - 2K_{0T}^{S'} \right]$$

$$+ \left[\beta \gamma_0 T \left(\frac{K_0^T}{K_0^S} \right) \right]^2 \left[K_{0T}^{S'} - 1 - \frac{1}{\beta^2} \left(\frac{\partial \beta}{\partial T} \right)_0 \right]$$

$$K_{0S}^{T'} = K_{0T}^{T'} + \left(\frac{\partial K^T}{\partial T} \right)_0 \left(\frac{\gamma_0^T}{K_0^S} \right)$$

$$\left(\frac{\partial K^S}{\partial T} \right)_S = \left(\frac{\partial K^S}{\partial T} \right)_0 + K_{0T}^{S'} \left(\frac{K_0^S}{\gamma_0^T} \right)$$

$$\left(\frac{\partial K^T}{\partial T} \right)_0 = \frac{\left(\frac{\partial K^S}{\partial T} \right)_0 - \beta \gamma_0 K_0^T - \beta T K_0^T \left(\frac{\partial \gamma}{\partial T} \right)_0 - \gamma_0 T K_0^T \left(\frac{\partial \beta}{\partial T} \right)_0}{(1 + \beta \gamma_0^T)}$$

$$\left(\frac{\partial K^T}{\partial T} \right)_S = \left(\frac{\partial K^T}{\partial T} \right)_0 + K_{0T}^{T'} \left(\frac{K_0^S}{\gamma_0^T} \right)$$

$$G_0^T = G_0^S = G_0$$

$$G_{0T}^{T'} = G_{0T}^{S'} = G_{0T}'$$

MSL-70-23, Vol. V

$$G'_{0S} = G'_{0T} + \left(\frac{\partial G}{\partial T} \right)_0 \left(\frac{\gamma_0 T}{K_0^S} \right)$$

$$\left(\frac{\partial G}{\partial T} \right)_S = \left(\frac{\partial G}{\partial T} \right)_0 + G'_{0T} \left(\frac{K_0^S}{\gamma_0 T} \right)$$

APPENDIX B

GRUNEISEN PARAMETER ESTIMATES

1. The Gruneisen parameter is defined thermodynamically as

$$\gamma = - \frac{1}{\rho c_p} \left(\frac{\partial V}{\partial T} \right) P \left(\frac{\partial P}{\partial V} \right)_S = \frac{\beta K_S}{\rho c_p}$$

For an isotropic elastic solid, this becomes

$$\gamma = \frac{\beta}{c_p} \left(c_L^2 - \frac{4}{3} c_S^2 \right)$$

Substituting appropriate values for copper gives

$$\gamma_0 = 2.13$$

2. Slater developed a relation that was an extension of the Debye Theory for a three-dimensional continuum, and assumed Poisson's ratio was independent of volume and γ is the same for all vibrational frequencies:

$$\gamma = - \frac{V}{2} \left(\frac{\partial^2 P / \partial V^2}{\partial F / \partial V} \right) - \frac{2}{3}$$

which simplifies at zero pressure to

MSL-70-23, Vol. V

$$\gamma_0 = \frac{1}{2} \left(K_{0S}' - \frac{1}{3} \right) = 2S - \frac{2}{3}$$

where S is from $U_S = C_B + S u_p$.

Ultrasonic data gives $S = 1.60$ and $\gamma = 2.53$.

Shock wave data gives $S = 1.53$ and $\gamma = 2.39$.

3. Dugdale and MacDonald give an expression for plane wave velocity vs. volume in a three-dimensional continuum that leads to an expression for γ differing from Slater's by a constant (1/3):

$$\gamma = - \frac{V}{2} \left(\frac{\partial^2 P / \partial V^2}{\partial P / \partial V} \right) - 1$$

which simplifies at zero pressure to

$$\gamma_0 = \frac{1}{2} \left(K_{0S}' - 1 \right) = 2S - 1$$

From ultrasonic data, $\gamma = 2.20$.

From shock wave data, $\gamma = 2.06$.

4. Anderson and Dienes give expressions for γ in terms of the longitudinal and shear modes of wave propagation:

$$\gamma_L = \frac{1}{3} + \frac{K_0^T}{C_L} \left(\frac{dC_L}{dP} \right)_0$$

$$\gamma_S = \frac{1}{3} + \frac{K_0^T}{C_S} \left(\frac{dC_S}{dP} \right)_0$$

Ultrasonic data gives $\gamma_L = 2.31$ and $\gamma_S = 1.82$.

5. Schuele and Smith give expressions for the "low-temperature" and "high-temperature" Gruneisen ratio, where low-temperature is the range in which it is assumed the solid behaves as a continuum and high-temperature is the range where all vibrational modes are excited and γ is constant:

$$\gamma_{LT} = \frac{1}{2+\epsilon^3} \left(\epsilon^3 \gamma_L + 2\gamma_S \right)$$

$$(\epsilon = C_S/C_L)$$

$$\gamma_{HT} = \frac{1}{3} \left(\gamma_L + 2\gamma_S \right)$$

Using ultrasonic data and γ_L and γ_S from above gives

$$\gamma_{LT} = 1.84 \text{ and } \gamma_{HT} = 1.98.$$

MSL-70-23, Vol. V

6. Perry calculated the Grueisen parameter from laser interferometer data obtained for electron beam energy deposition.* For polycrystalline copper, he obtained $\gamma = 1.63$ assuming instantaneous deposition and $\gamma = 1.93$ assuming 50 nsec deposition time.

(All of the ultrasonics data used in this appendix are for zero pressure and 20°C).

* Perry, F. C., "Thermoelastic Response of Polycrystalline Metals to Relativistic Electron Beam Absorption", J. Appl. Phys., Vol. 41, p. 5017-5022, 1970.

APPENDIX C

GRUNEISEN PARAMETER, PRESSURE DERIVATIVE

1. Thermodynamic Relation -

$$\gamma = \frac{\beta K^S}{\rho c_p}$$

$$\left(\frac{\partial \gamma}{\partial P} \right)_T = \gamma_0 \left[\frac{1}{\beta} \left(\frac{\partial \beta}{\partial P} \right)_T + \frac{1}{K^S} \left(\frac{\partial K^S}{\partial P} \right)_T - \frac{1}{\rho} \left(\frac{\partial \rho}{\partial P} \right)_T - \frac{1}{c_p} \left(\frac{\partial c_p}{\partial P} \right)_T \right]$$

This can be simplified by using: *

$$\left(\frac{\partial \beta}{\partial P} \right)_T = \left(\frac{1}{K^T} \right)^2 \left(\frac{\partial K^T}{\partial T} \right)_P$$

$$\left(\frac{\partial \rho}{\partial P} \right)_T = \frac{\rho}{K^T}$$

$$\left(\frac{\partial c_p}{\partial P} \right)_T = - \frac{T}{\rho} \left[\left(\frac{\partial \beta}{\partial T} \right)_P + \beta^2 \right]$$

* See, e.g. Thurston, R. N., "Ultrasonic Data and the Thermodynamics of Solids", IEEE Proc., Vol. 53, p. 1320-1336, 1965.

MSL-70-23, Vol. V

to give:

$$\left(\frac{\partial \gamma}{\partial P} \right)_T = \gamma_0 \left[-\frac{1}{\beta K^T} \left(\frac{\partial K^T}{\partial T} \right)_P + \frac{1}{K^S} \left(\frac{\partial K^S}{\partial P} \right)_T - \frac{1}{K^T} + \frac{T}{c_p \rho} \left\{ \left(\frac{\partial \beta}{\partial T} \right)_P + \beta^2 \right\} \times 23.9 \right]$$

This can be modified to:

$$\left(\frac{\partial \gamma}{\partial P} \right)_T = \frac{\gamma_0}{K^S} \left[\left(\frac{\partial K^S}{\partial P} \right)_T + \frac{1}{\beta K^T} \left(\frac{\partial K^S}{\partial T} \right)_P - 1 - \gamma - T \left(\frac{\partial \gamma}{\partial T} \right)_P \right]$$

2. Constant γ/V :

$$\frac{\gamma}{V} = \frac{\gamma_0}{V_0} \quad \text{or} \quad \gamma = \rho_0 \gamma_0 V$$

$$\left(\frac{\partial \gamma}{\partial P} \right)_T = \rho_0 \gamma_0 \left(\frac{\partial V}{\partial P} \right)_T$$

$$\text{but} \quad \left(\frac{\partial V}{\partial P} \right)_T = -\frac{1}{\rho^2} \left(\frac{\partial \rho}{\partial P} \right)_T = -\frac{1}{\rho K^T}$$

$$\text{so} \quad \left(\frac{\partial \gamma}{\partial P} \right)_T = -\frac{\rho_0 \gamma_0}{\rho K^T}$$

Letting $\sigma = \sigma_0 \left(\frac{K_0^T + K_{0T}^{T'} P}{K_0^T} \right)^{1/K_{0T}^{T'}}$

and $K^T = K_0^T + K_{0T}^{T'} P$

gives:

$$\left(\frac{\partial \gamma}{\partial P} \right)_T = \frac{\gamma_0}{\left(\frac{1}{K_0^T} \right)^{\left(1/K_{0T}^{T'} \right)} \left(K_0^T + K_{0T}^{T'} P \right)^{\left(1+K_{0T}^{T'} \right)/K_{0T}^{T'}}$$

At $P = 0$, this reduces to

$$\left(\frac{\partial \gamma}{\partial P} \right)_T = - \frac{\gamma_0}{K_0^T}$$

MSL-70-23, Vol. V

APPENDIX D

DEVIATORIC STRESS ESTIMATES

The shock wave equation of state for copper is given by:

$$\left. \begin{aligned} \sigma_H &= 1.5 + 344 u_p + 143 u_p^2 \\ \sigma_H &= 3.1 + 1308\mu + 3520\mu^2 \\ P_H &= 1308\mu + 3520\mu^2 \text{ (Hydrostat)} \end{aligned} \right\} \quad (D-1)$$

where $\mu = (v_0/v) - 1$.

The deviatoric stress (σ_D) can be defined as the difference between the dynamic stress-compression path ($\sigma_H - \mu$) and the hydrostat, and is a measure of the material's ability to support shear. If the material strain hardens, the deviatoric stress will be a function of μ . In Equation D-1, σ_D was assumed constant at 3.1 kbar which gives $P_H = \sigma_H - 3.1$.

The deviatoric stress can also be estimated from uniaxial stress data, shock wave data or ultrasonics data as follows:

$$\sigma_D = \sigma_H - P_H = \frac{2}{3} Y \quad (D-2)$$

where Y is flow stress under uniaxial stress conditions.

A. The flow stress at low strain rate from the uniaxial stress tests (see Figure 3) is ~ 3 kbar, which gives $\sigma_D = 2$ kbar.

B. For a hugoniot elastic limit (σ_e) of 8 kbar, the relation $Y = \sigma_e (1-2v/l-v)$ gives $Y = 3.6$ kbar. From Equation D-2, $\sigma_D = 2.4$ kbar.

C. Since σ_D can also be taken as the difference between σ_H and P_H at a compression corresponding to the hugoniot elastic limit, one has

$$\sigma_D = \sigma_H - P_H = \sigma_e - P_e$$

where

$$\sigma_e = \rho_0 C_L^2 \left(\frac{\mu_e}{1+\mu_e} \right) = 2018 \left(\frac{\mu_e}{1+\mu_e} \right)$$

$$P_e = \rho_0 C_B^2 \left(\frac{\mu_e}{1+\mu_e} \right) = 1418 \left(\frac{\mu_e}{1+\mu_e} \right)$$

For $\sigma_e = 8$ kbar: $\mu_e = 0.004$ and $P_e = 5.7$ kbar. This gives $\sigma_D = 2.3$ kbar.

The agreement of these estimates with the value of 3.1 kbar from Equation D-1 is considered good, taking into account the assumptions underlying each method and the experimental inaccuracies.

Also, it should be noted that the stress-axis intercept is larger in the $\sigma_H - \mu$ plane than the $\sigma_H - u_p$ plane. Assuming linear elastic and hydrostatic behavior up to the elastic limit, then:

MSL-70-23, Vol. V

 $\sigma_H - u_p$ plane -

$$\sigma_{D_u} = \rho_0 u_e (C_L - C_B)$$

 $\sigma_H - \mu$ plane -

$$\sigma_{D_\mu} = \frac{\mu_e}{1+\mu_e} \left(\rho_0 C_L^2 - \rho_0 C_B^2 \right)$$

Using the approximations $u_e \approx \mu_e/C_L$ and $\mu_e \approx \mu_e/(1+\mu_e)$,
and subtracting:

$$\Delta\sigma_D = \sigma_{D_u} - \sigma_{D_\mu} = \rho_0 C_B \mu_e (C_L - C_B)$$

For $\sigma_e = 8$ kbar, $\mu_e = 0.004$ and $\Delta\sigma_D = 1.1$ kbar, compared to
 $\Delta\sigma_D = 1.6$ kbar from $\sigma_H - u_p$ and $\sigma_H - \mu$ given in Equation D-1.

APPENDIX E

EQUATIONS OF STATE, ULTRASONICS

Numerous analytical and empirical relations have been developed for determining equations of state from ultrasonics data. Some of these are presented here.

1. The Birch equation of state for the isotherm can be expressed as:

$$P_T = \frac{3}{2} K_0^T \left[\left(1+\mu \right)^{7/3} - \left(1+\mu \right)^{5/3} \right] \left[1-\xi \left\{ \left(1+\mu \right)^{2/3} - 1 \right\} \right]$$

$$\text{where } \xi = \frac{12-3 K_{0T}^{T'}}{4}$$

$$P_T = 2060 \left[\left(1+\mu \right)^{7/3} - \left(1+\mu \right)^{5/3} \right] \left[1+1.19 \left\{ \left(1+\mu \right)^{2/3} - 1 \right\} \right]$$

* Another parameter sometimes used with this equation of state is

$$\alpha \left[\left(1+\mu \right)^{2/3} - 1 \right]^2$$

$$\text{where } \alpha = \frac{3}{8} \left[K_0^T K_{0T}^{T''} - 7 K_{0T}^{T'} + \left(K_{0T}^{T'} \right)^2 + \frac{143}{9} \right]$$

However, this term can usually be neglected, contributing <0.5% at 100 kbar for copper.

MSL-70-23, Vol. V

2. The Murnaghan equation of state is derived by assuming the bulk modulus is linear with pressure which gives:

$$\text{Isotherm } \cdot P_T = \frac{K_0^T}{K_{0T}^{T'}} \left[\left(1+\mu \right)^{K_{0T}^{T'}} - 1 \right]$$

$$P_T = 245.6 \left[\left(1+\mu \right)^{5.59} - 1 \right]$$

$$\text{Adiabat } - P_S = \frac{K_0^S}{K_{0S}^{S'}} \left[\left(1+\mu \right)^{K_{0S}^{S'}} - 1 \right]$$

$$P_S = 262.6 \left[\left(1+\mu \right)^{5.40} - 1 \right]$$

3. Instead of a linear bulk modulus-pressure relation, Keane assumed:

$$dK^S = \left[\frac{\left(\frac{K_0^{S'} - K_\infty^{S'}}{K_0^S} \right) K_0^S}{K_\infty^{S'}} + K_\infty^{S'} \right] dP$$

where $K_\infty^{S'}$ is the limiting value of K^S at very high pressure.

This leads to:

$$P_S = \frac{K_0^S K_{0S}^{S'}}{\left(K_\infty^{S'} \right)^2} \left[\left(1+\mu \right)^{K_\infty^{S'}} - 1 \right] - \frac{\left(\frac{K_0^{S'} - K_\infty^{S'}}{K_0^S} \right) K_0^S}{K_\infty^{S'}} \ln \left(1+\mu \right)$$

Anderson⁽³⁶⁾ suggested that this equation be applied by empirically determining $K_{\infty}^{S'}$. This can be done by evaluating the equation at a known high pressure shock wave point, i.e., the equation is solved for $K_{\infty}^{S'}$ at a known P_S , μ point. Evaluating the high pressure hugoniot given by Equation 14 at $P_H = K_0^S = 1418$ kbar gives $\mu = 0.443$. This value of P_H corresponds to $P_S = 1371$ kbar, using the entropy correction term suggested by Duvall⁽³⁷⁾ for the Murnaghan equation. Solving the above equation for $K_{\infty}^{S'}$ at $P_S = 1371$ kbar and $\mu = 0.443$ gives

$$K_{\infty}^{S'} = 3.7$$

$$\therefore P_S = 559.3 \left[\left(1+\mu \right)^{3.7} - 1 \right] - 651.5 \ln \left(1+\mu \right)$$

Huang* gives the upper bound for $K^{S'}$ as:

$$K_{\infty}^{S'} = 4S - \frac{11}{3} = K_{0S}^{S'} - \frac{8}{3} = 2.73$$

This gives:

$$P_S = 1025 \left[\left(1+\mu \right)^{2.73} - 1 \right] - 1383 \ln \left(1+\mu \right)$$

* Huang, Y. K., "Analytical Approach to the Shock Compressibility of 18 Cubic-Lattice Metals", J. Chem. Phys., Vol. 53, p. 571-575, 1970.